

AD-A093 155

GREAT LAKES SCIENCES INC AMHERST NY  
TARGENT GLINT SUPPRESSION TECHNOLOGY.(U)  
SEP 80 A J CECERE, R A PADGUG, M D BURNS

F/6 17/9

F30602-79-C-0141

UNCLASSIFIED

GLS-80-05

RADC-TR-80-303

NL

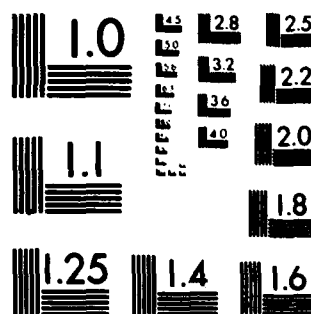
END

DATE

FILED

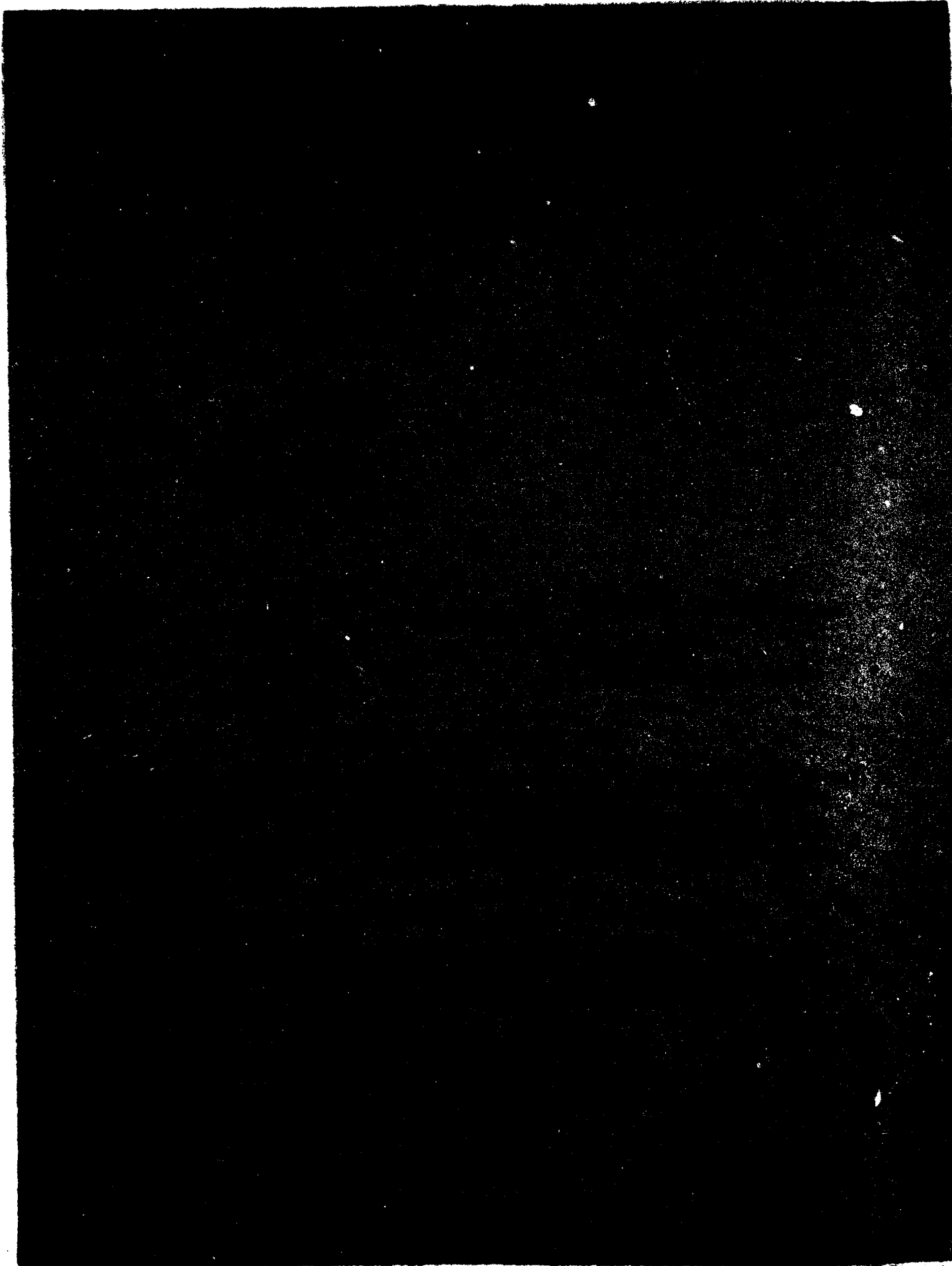
1-8

OTIC



MICROCOPY RESOLUTION TEST CHART  
NATIONAL BUREAU OF STANDARDS 1963 A

AD A093155



UNCLASSIFIED

SECURITY CLASSIFICATION OF THIS PAGE (When Data Entered)

1. REPORT DOCUMENTATION PAGE		READ INSTRUCTIONS BEFORE COMPLETING FORM	
1. REPORT NUMBER RADG-TR-80-303 / L	2. GOVT ACCESSION NO. AD-A093	3. RECIPIENT'S CATALOG NUMBER 755	
4. TITLE (and Subtitle) TARGET GLINT SUPPRESSION TECHNOLOGY.	5. TYPE OF REPORT & PERIOD COVERED Final Technical Report. April 79 - April 80	6. PERFORMING ORG. REPORT NUMBER GLS-80-057	
7. AUTHOR(s) A. J. / Cecere R. A. / Padgug	8. CONTRACT OR GRANT NUMBER(s) F30602-79-C-0141		
9. PERFORMING ORGANIZATION NAME AND ADDRESS Great Lakes Sciences, Inc. 331 Alberta Drive Amherst NY 14226	10. PROGRAM ELEMENT, PROJECT, TASK AREA & WORK UNIT NUMBERS 62702F 45061343		
11. CONTROLLING OFFICE NAME AND ADDRESS Rome Air Development Center (OCTM) Griffiss AFB NY 13441	12. REPORT DATE September 1980	13. NUMBER OF PAGES 89	
14. MONITORING AGENCY NAME & ADDRESS (if different from Controlling Office) Same	15. SECURITY CLASS. (of this report) UNCLASSIFIED	15a. DECLASSIFICATION DOWNGRADING SCHEDULE N/A	
16. DISTRIBUTION STATEMENT (of this Report) Approved for public release; distribution unlimited.			
17. DISTRIBUTION STATEMENT (of the abstract entered in Block 20, if different from Report) Same			
18. SUPPLEMENTARY NOTES Project Engineer: Capt D. E. Stein (OCTM)			
19. KEY WORDS (Continue on reverse side if necessary and identify by block number) Radar Measurement Errors      Pointing Errors Target Glint Effects      Tracking Errors Rayleigh Targets Detection/Estimation Airborne Target Models			
20. ABSTRACT (Continue on reverse side if necessary and identify by block number) The subject of target noise effects, such as radar glint and the analogous radar range measurement error, is addressed both theoretically and via computer simulation. A thorough analytic treatment for Rayleigh targets is presented, including optimum target noise reduction techniques and associated variances. Performance against representative aircraft and cruise missile models is also presented.			

DD FORM 1473 EDITION OF 1 NOV 65 IS OBSOLETE

UNCLASSIFIED

SECURITY CLASSIFICATION OF THIS PAGE (When Data Entered)

394230

JOK

UNCLASSIFIED

SECURITY CLASSIFICATION OF THIS PAGE(When Data Entered)



UNCLASSIFIED

SECURITY CLASSIFICATION OF THIS PAGE(When Data Entered)

## TABLE OF CONTENTS

<u>Section</u>	<u>Page</u>
1 INTRODUCTION & SUMMARY.....	1
2 TARGET DETECTION STUDIES.....	3
2.1 Target Model.....	3
2.1.1 Amplitude Characterization.....	3
2.1.2 Spatial Characterization.....	5
2.2 Effects of Signal Correlation.....	7
2.3 Operational Implications.....	8
3 TARGET LOCATION STUDIES.....	12
3.1 Location Measurement Components.....	12
3.2 Theoretical Results.....	13
3.2.1 Monopulse Preliminaries.....	15
3.2.2 Variance Expressions.....	17
3.2.3 Adaptive Frequency Slection.....	26
3.3 Simulation Results.....	34
3.3.1 Target Scattering Models.....	34
3.3.1.1 Aircraft Scattering Model.....	35
3.3.1.2 Cruise Missile Model.....	40
3.3.1.3 Comparisons With Rayleigh Model.....	48
3.3.2 Simulation Description.....	50
3.3.3 Simulation Statistics.....	56
3.3.3.1 Aircraft Statistics.....	56
3.3.3.2 Cruise Missile Statistics.....	60
3.4 Operational Implications.....	65
4 KEY FINDINGS AND RECOMMENDATIONS.....	67
APPENDIX A.1 Derivation of Correlation Coefficient.....	69
APPENDIX A.2 Noncoherent Integration.....	70
APPENDIX A.3 Distribution of Monopulse Statistics.....	74
APPENDIX A.4 High SNR Approximations to $w^2$ .....	78
APPENDIX A.5 M.L.E. of Monopulse Angle.....	79

## EVALUATION

This effort, in support of TPO IC2a, Aircraft Identification, was a study to assess the relative effectiveness of various glint-error suppression techniques in radar systems. Methods of pulse-to-pulse decorrelation investigated in this effort included frequency diversity, spatial diversity, temporal diversity, and polarization diversity. The feasibility of adaptive processing techniques was also assessed. This study has advanced our understanding of the phenomenology of both range and angle tracking errors. It has identified the significance of both types of errors as a function of target dimensions, geometry, and range. Finally, this study has identified the optimum decorrelation techniques and associated signal processing techniques for minimizing target glint-induced errors. Although the study was performed for CW radar systems, the results are also applicable to narrow-pulse, high resolution radars.

*David E. Stein*  
 DAVID E. STEIN, Capt, USAF  
 Project Engineer

Accession For	
NTIS GRA&I	<input checked="" type="checkbox"/> <input type="checkbox"/> <input type="checkbox"/>
DDC TAB	
Unannounced Justification	
By _____	
Distribution/ _____	
Availability Codes	
Dist.	Avail and/or special
<i>HA</i>	



## 1. INTRODUCTION AND SUMMARY

An analysis of target noise effects, with particular emphasis on target-induced radar positional measurement errors, was conducted. Several new and significant findings were derived for Rayleigh targets and shown to be applicable to complex targets, such as aircraft, via a detailed simulation analysis.

For such targets, the target noise effects were shown to be controlled by the target's RCS centroid and second central moment  $W_0^2$ , in the radar measurement dimension of interest. The RCS centroid was shown to determine the mean target location under high signal-to-noise conditions. Assuming  $N$  independent radar measurements are averaged, the Cramer-Rao bound on the resultant positional variance was shown to be  $W_0^2/2N$ . In situations where it is practical to implement a weighted average, RCS weighting was shown to be optimum and results in a measurement variance of  $W_0^2/2(N-1)$ . For those applications in which such weighting is impractical, data editing with an RCS threshold of six tenths of the mean target RCS was shown extremely effective and results in a variance of  $1.5W_0^2/2N$ .

For non-Rayleigh targets, such as a simple two scatterer target, RCS weighting was shown to be effective but not optimum. While this was not pursued to any great extent, a heavier RCS weighting appeared preferable. In such situations a technique previously reported in the literature\* proved better than RCS weighting.

This report is organized into two principal sections. Section 2 addresses the impact of target effects on the noncoherent detection problem associated with search radars. Generally speaking, target detection was shown to degrade with increasing pulse-to-pulse correlation. Temporal and frequency diversity techniques for decorrelating the target signal were shown to depend on the target parameter  $W_0^2$  in the cross-range and range dimension

---

\* Loomis, J.M. and Graf, E.R., "Frequency-Agile Processing to Reduce Glint Pointing Error," Trans. IEEE, vol. AES-10, Nov. 1974. pp. 811-820.

respectively. For representative operational conditions, frequency diversity was shown to be the preferable technique.

Section 3, which deals with the target location studies, represents the major study emphasis. Analytic derivations and computer simulation validation of the key results cited earlier are presented.

## 2. TARGET DETECTION STUDIES

In this section the role of waveform diversity in enhancing fluctuating target detection is addressed. The principal finding is that frequency diversity rather than temporal diversity is the most effective means of enhancing target detection.

### 2.1 Target Model

2.1.1 Amplitude Characterization. Since the target detection study was analytic in nature, an analytic description of a representative target radar cross section (RCS) model was required. In this section a very brief motivation and description of the selected target model is presented.

The targets of interest to this study are principally aircraft which are highly complex targets having many scattering centers. For such targets a Rayleigh target amplitude fluctuation model is usually quite representative and was assumed for this study. While this distribution results from the assumption of an infinite number of equal scattering centers, the assumption is really quite representative when the number of near equal scattering centers is as small as 4 to 6.

This result can be justified by observing the data presented in Figure 1. Here the target RCS was assumed to be the sum of  $N$  independent equal amplitude scatterers, normalized such that the average RCS is unity, i.e.

$$RCS_N = \frac{1}{N} \left| \sum_{n=1}^N \text{EXP}(j\phi_n) \right|^2$$

where  $\phi_n$  are independent random variables uniformly distributed over  $(0, 2\pi)$ . The cumulative distribution plotted in the figure is \*

$$\begin{aligned} P(x) &= P(RCS_N \leq x) \\ &= \sqrt{xN} \int_0^{\infty} \left[ J_0(y) \right]^N J_1(\sqrt{xN} y) dy \end{aligned}$$

---

\* Greenwood, J.A., "The Distribution of Length and Components of the Sum of  $n$  Random Unit Vectors", Annals of Mathematical Statistics, Vol. 26, No. 2, June 1955.

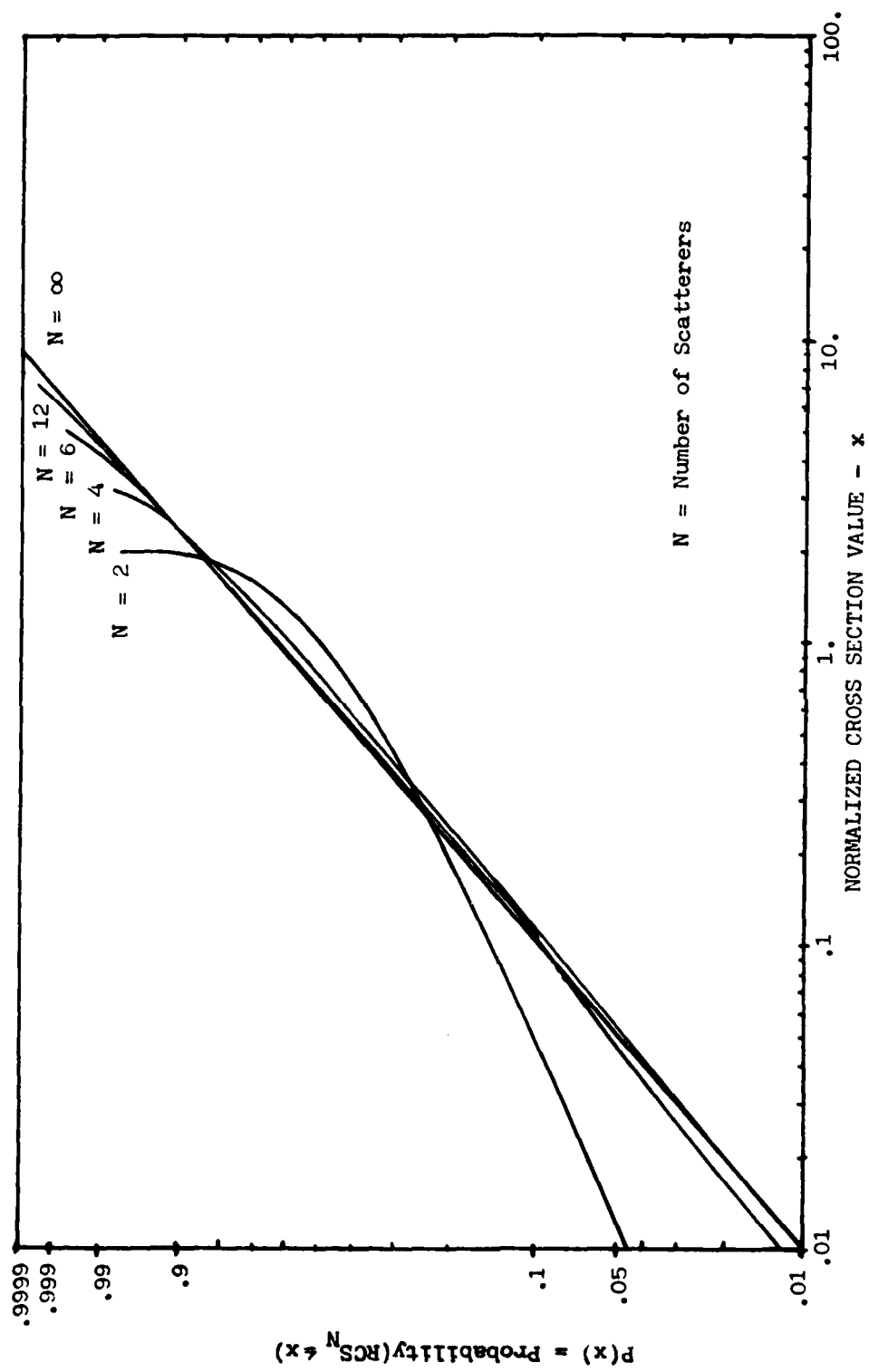


Figure 1. CUMULATIVE RCS DISTRIBUTION

Here one notes that for  $N$  equal to 4 to 6, a good fit to the Rayleigh distribution ( $N = \infty$ ) is achieved. Since it seemed plausible that a generic A/C model would contain at least 4 to 6 comparable scattering centers, the Rayleigh target model was selected. (Note: In Section 3.2.1 the cross section distribution resulting from a detailed aircraft model is shown to be effectively Rayleigh for either horizontal or vertical polarization).

2.1.2 Spatial Characterization. Before the effects of diversity on target detection can be addressed, the target must also be described in terms of its spatial distribution as illustrated in Figure 2. This characterization will also be necessary for the theoretical assessment of target induced radar measurement errors such as glint (see Section 3.2). Here the complex scattering amplitude arising from a point  $(x,y)$  on the target of Figure 2 is

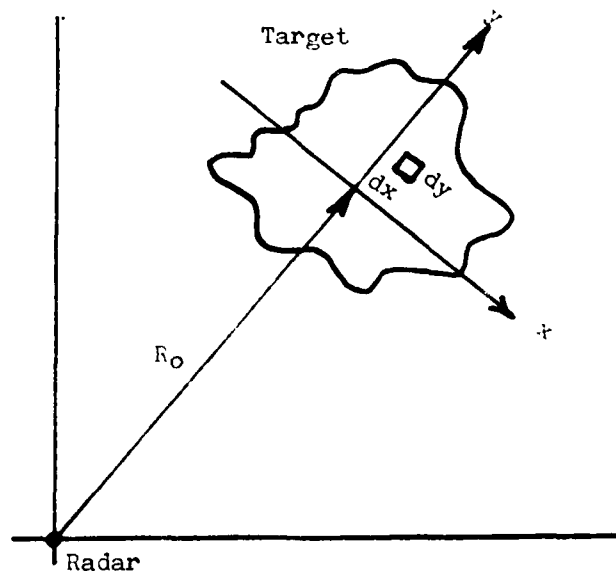


Figure 2 Rough Radar Target

represented by  $a(x,y)$ . Further assume that scattering from any differential element is totally independent from any other element, has random phase and the expected power can be defined by a function  $s(x,y)$ , where:

$$E \left[ a(x_1, y_1) a^*(x_2, y_2) \right] = s(x_1, y_1) \delta(x_2 - x_1, y_2 - y_1)$$

Here  $\delta$  represents the Dirac delta - function.

If the target extremes are denoted by  $\pm W_x/2$  and  $\pm W_y/2$ , then the complex narrowband return signal at frequency  $f$  can be represented as

$$A(f) = \text{EXP}(-j4\pi R_0 f/c) \int_{-\frac{1}{2}W_x}^{\frac{1}{2}W_x} \int_{-\frac{1}{2}W_y}^{\frac{1}{2}W_y} a(x,y) \text{EXP}(-j4\pi y f/c) dx dy$$

This signal is assumed to be a circular (i.e. complex) Gaussian process since it is the sum of many random elements. As a result its amplitude distribution is Rayleigh, which is in keeping with the assumptions of Section 2.1.1.

With this signal representation the correlation parameters of the process in frequency, time or space can be addressed. First consider the correlation between two signals at different center frequencies. Defining the correlation coefficient as

$$\begin{aligned} \rho &= \frac{E \left[ A(f_1) A^*(f_2) \right]}{E \left[ |A(f_1)|^2 \right]} \\ &= \frac{\iint s(x,y) \text{EXP} \left[ -j4\pi y (f_1 - f_2)/c \right] dx dy}{\iint s(x,y) dx dy} \end{aligned}$$

and a normalized range scattering function  $S_y(y)$  as

$$S_y(y) = \frac{\int s(x,y) dx}{\iint s(x,y) dx dy}$$

the frequency correlation coefficient becomes

$$\begin{aligned} p(B) &= \int S_y(y) \text{EXP}(-j2\pi B y) dy \\ &\approx p(0) + B p'(0) + \frac{1}{2} B^2 p''(0) \\ &= 1 - j2\pi B \int y S_y(y) dy - 2\pi^2 B^2 \int y^2 S_y(y) dy \end{aligned}$$

for small values of  $B = 2(f_1 - f_2)/c$ . Assuming the target measurements were made at a range  $R_0$  corresponding to the range RCS centroid of the target, then  $p'(0)$  is zero and  $p(B)$  is real and approximated by

$$p(B) = 1 - 2\pi^2 B^2 \int y^2 S_y(y) dy$$

As a result the correlation coefficient in frequency is seen to be controlled by the second central moment of the normalized range scattering function.

In an analogous manner the correlation coefficient for target rotation can also be derived. Here two target samples are assumed taken with the second delayed in time by an amount  $t$ . During this time interval the target is assumed to rotate through an angle  $\theta = \omega_R t$ . In this case one finds:

$$p(\xi) = 1 - 2\pi^2 \xi^2 \int x^2 S_x(x) dx$$

where  $S_x(x)$  is the normalized cross range scattering function and  $\xi = 2f\omega_R t/c$ . Here the angular or temporal correlation function is seen to be controlled by the second moment of the normalized cross range scattering function. Details of this derivation are contained in Appendix A.1.

**2.2 Effects of Signal Correlation.** In this subsection the effects of signal correlation on target detection are addressed. A Rayleigh target model with varying pulse-to-pulse correlation is assumed. The target statistics then lie between those of a Swerling I model for unity pulse-to-pulse correlation and a Swerling II model for zero pulse-to-pulse correlation. Results are presented for a scanning search radar which is assumed to noncoherently integrate  $N$  pulses. Generally speaking, detection performance is shown to be a maximum when the pulse-to-pulse correlation is a minimum. As a result noncoherent search radars should routinely utilize pulse-to-pulse

frequency agility to decorrelate target statistics and thereby maximize target detection.

For a Rayleigh target the following expressions for the probability of detection and false alarm were derived (see Appendix A.2):

$$P_D = \sum_{m=1}^M \frac{\text{EXP}(-\gamma/\theta_m)}{\prod_{\substack{k=1 \\ k \neq m}}^M (1 - \frac{\theta_k}{\theta_m})}$$

$$P_{FA} = \text{EXP}(-2\gamma/N_o) \sum_{m=0}^{M-1} \frac{(2\gamma/N_o)^m}{m!}$$

where

- M = Number of Pulses Integrated
- $\gamma$  = Threshold Level
- $N_o$  = Noise Power
- $\theta_m$  = The  $m^{\text{th}}$  Eigenvalue of the Received Signal Covariance Matrix

The expression for  $P_D$  assumes that the eigenvalues are distinct and must be modified to handle the case of repeated eigenvalues.

Figure 3 is a plot of  $P_D$  vs the interpulse correlation coefficient for  $M = 2, 4$  and  $8$  pulses and signal-to-noise ratios of 3, 6 and 9 db when the false alarm probability is  $10^{-4}$ . Aside from the case of  $M = 2$  with  $SNR = 3$  db, detection performance is seen to increase with decreasing interpulse correlation. This trend is increasingly strong with increasing signal-to-noise ratios.

**2.3 Operational Implications.** Having derived expressions for the pulse-to-pulse target correlation in Section 2.1.2 and demonstrated in Section 2.2 that detection performance is maximized when the pulse-to-pulse correlation is minimized, we address the operational implications of these findings in this section. Frequency agility is shown to be the most practical means of decorrelating the received signal.



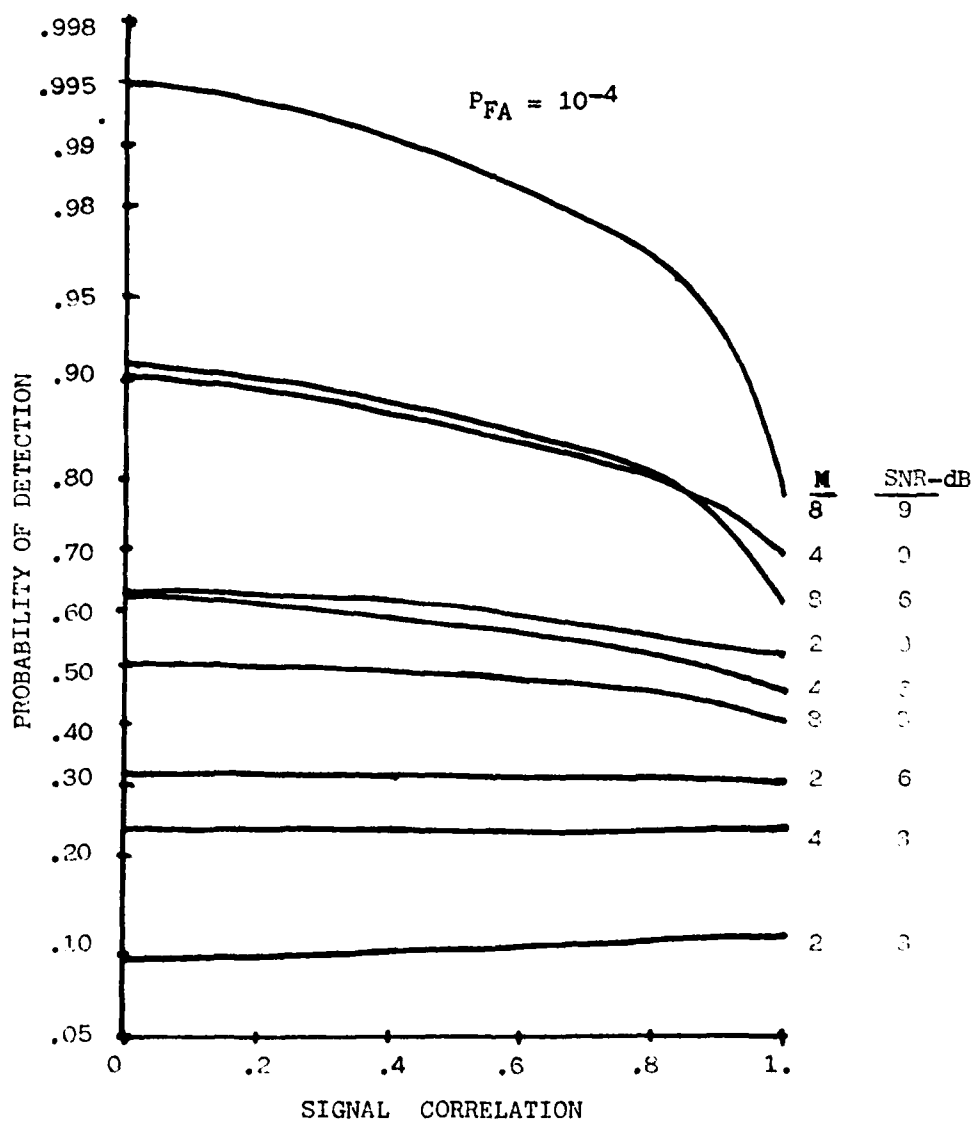


Figure 3 Correlation Effects on Detection

Assuming a pulse-to-pulse target correlation coefficient of .5 is desired, the expression for  $p(\beta)$  derived in section 2.1.2 may be set equal to .5. Noting  $\beta = 2\Delta f/c$ , one may solve for  $\Delta f$  as

$$\Delta f = \frac{.08c}{W_R} \text{ MHz}$$

where  $W_R^2$  is the second central moment of the target's RCS function in range. This relationship is graphed in Figure 4. Indicated on this figure are typical values of  $W_R$  in meters for both a representative cruise missile and fighter aircraft. These values were derived from the target models discussed in Section 3.3.1. For these values, pulse-to-pulse frequency agility requirements ranging from 4.5 to 15 MHz are noted. These values are well within the capabilities of current radars.

To determine temporal decorrelation requirements, the temporal correlation function derived in Section 2.1.2 is also set equal to .5. This yields

$$\Delta t = \frac{.08\lambda}{\omega_R W_x}$$

where  $\lambda$  is the radar wavelength,  $\omega_R$  is the angular rotation of the target relative to the radar line-of-sight, and  $W_x^2$  is the second central moment of the target's RCS function in the cross-range dimension. This relationship is shown in Figure 5 for a target rotational rate of  $1^\circ$  per second and radar wavelengths of .01 and .1 meters. The values of  $W_x$  indicated are also based on the target models discussed in Section 3.3.1. The resulting temporal decorrelation times are seen to exceed the interpulse period of representative search radars which typically run several hundred pulses per second. As a result the temporal decorrelation of targets will usually be too slow to provide uncorrelated returns. This temporal decorrelation should be adequate to provide scan-to-scan decorrelation.

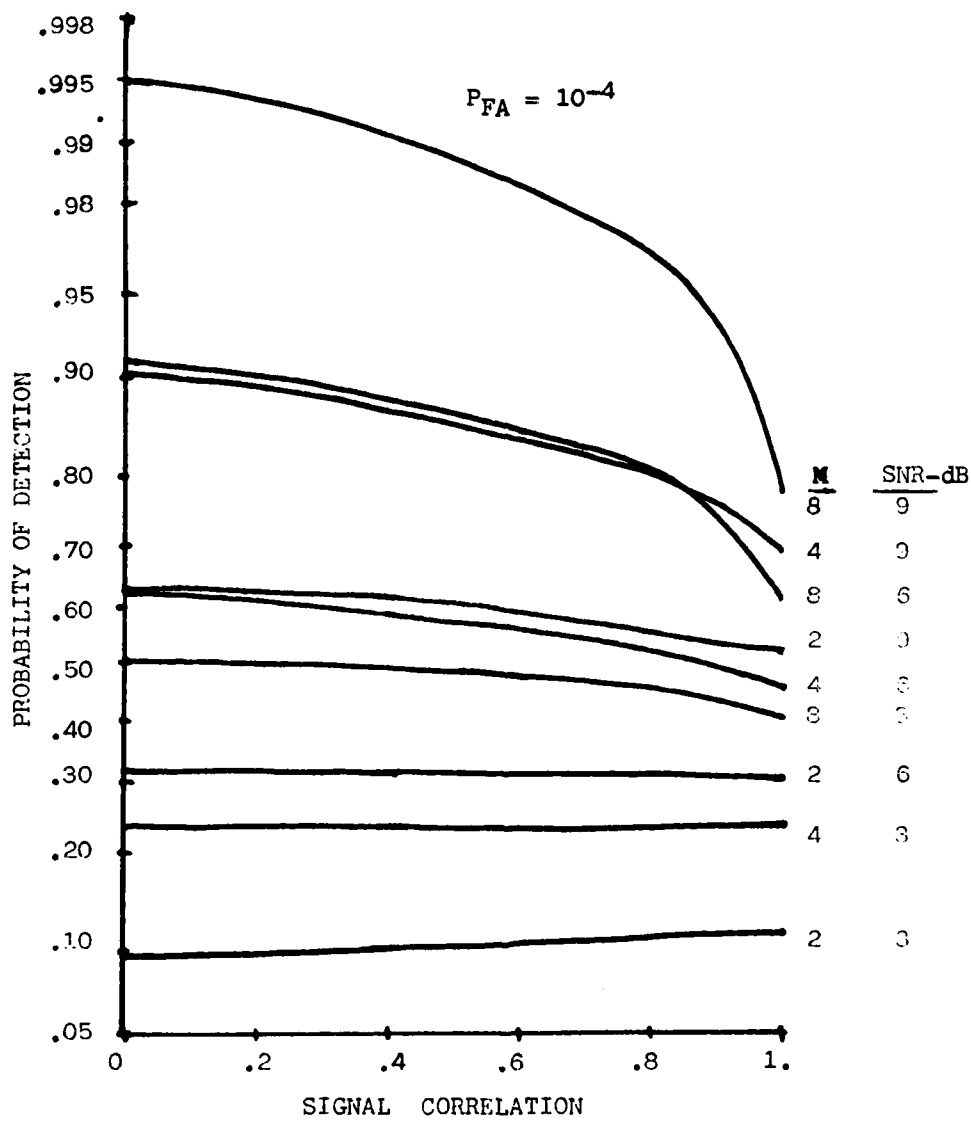


Figure 3 Correlation Effects on Detection

Assuming a pulse-to-pulse target correlation coefficient of .5 is desired, the expression for  $\rho(B)$  derived in section 2.1.2 may be set equal to .5. Noting  $B = 2\Delta f/c$ , one may solve for  $\Delta f$  as

$$\Delta f = \frac{.08c}{W_R} \text{ MHz}$$

where  $W_R^2$  is the second central moment of the target's RCS function in range. This relationship is graphed in Figure 4. Indicated on this figure are typical values of  $W_R$  in meters for both a representative cruise missile and fighter aircraft. These values were derived from the target models discussed in Section 3.3.1. For these values, pulse-to-pulse frequency agility requirements ranging from 4.5 to 15 MHz are noted. These values are well within the capabilities of current radars.

To determine temporal decorrelation requirements, the temporal correlation function derived in Section 2.1.2 is also set equal to .5. This yields

$$\Delta t = \frac{.08\lambda}{\omega_R W_x}$$

where  $\lambda$  is the radar wavelength,  $\omega_R$  is the angular rotation of the target relative to the radar line-of-sight, and  $W_x^2$  is the second central moment of the target's RCS function in the cross-range dimension. This relationship is shown in Figure 5 for a target rotational rate of  $1^\circ$  per second and radar wavelengths of .01 and .1 meters. The values of  $W_x$  indicated are also based on the target models discussed in Section 3.3.1. The resulting temporal decorrelation times are seen to exceed the interpulse period of representative search radars which typically run several hundred pulses per second. As a result the temporal decorrelation of targets will usually be too slow to provide uncorrelated returns. This temporal decorrelation should be adequate to provide scan-to-scan decorrelation.

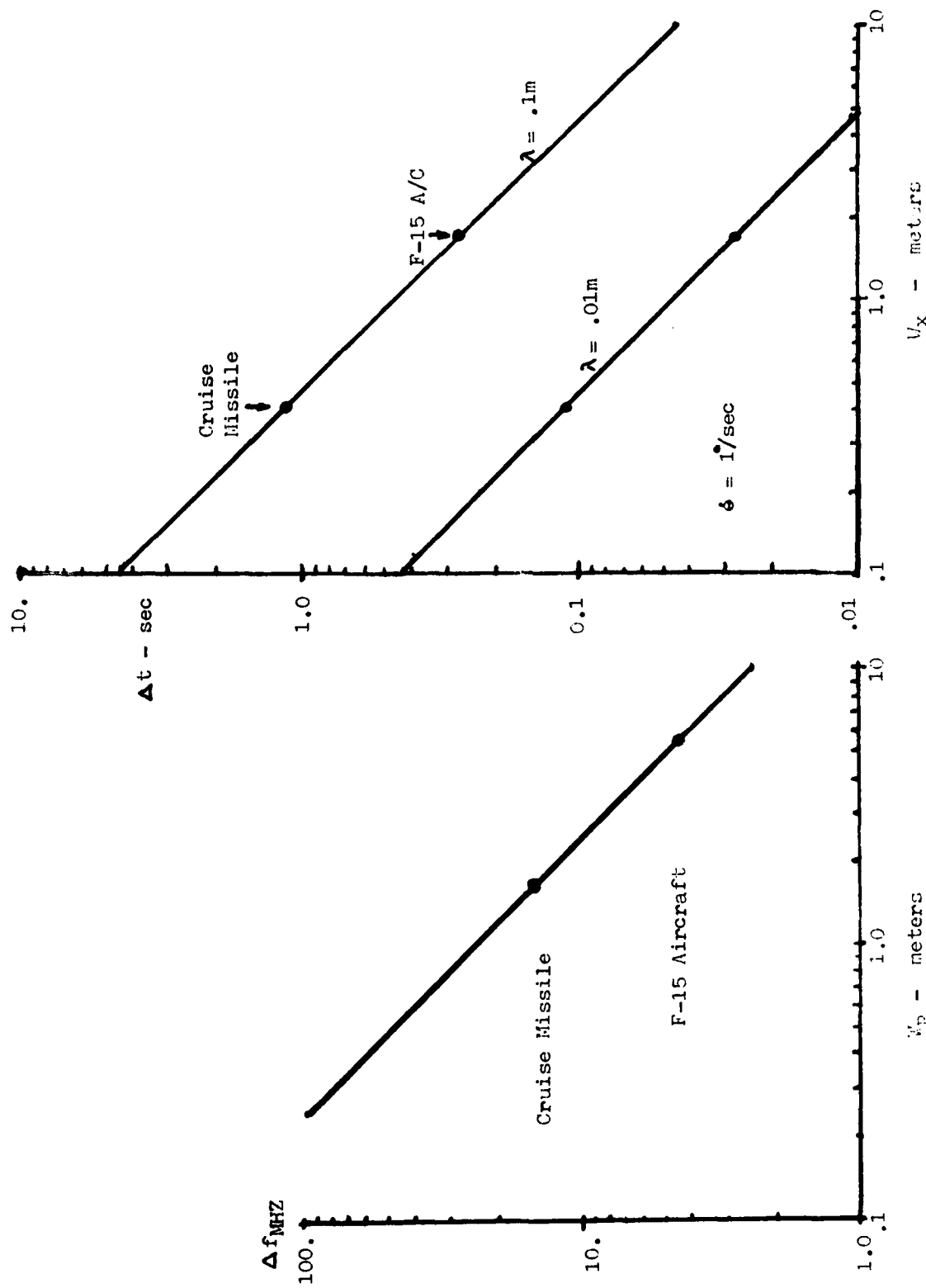


Figure 5 Temporal Diversity Requirements

Figure 4 Frequency Diversity Requirements

### 3. TARGET LOCATION STUDIES

3.1 Location Measurement Error Components. Before addressing the target noise component of the radar measurement error, it will be instructive to first review all the components of the location measurement error. Since the equations of motion which describe the dynamics of a target under track usually apply to its center-of-gravity (c.g.), it is useful to reference measurement errors to the target's c.g. If  $x$  is the measured target location (in range or angle and  $x_{cg}$  is the location of the target's center of gravity, the measurement error is then defined as

$$\begin{aligned}\epsilon &= x - x_{cg} \\ &= x_s + x_n + x_t\end{aligned}$$

Here the error is portrayed as having three components. The first component,  $x_s$ , is the limiting system error, or in other words the measurement error that would occur in determining the location of a constant point target with infinite SNR. This error results from system hardware limitations and is usually modeled as a zero mean error whose standard deviation is somewhere between  $1/50^{\text{th}}$  and  $1/25^{\text{th}}$  of the basic radar's measurement resolution,  $R$ .

The second term,  $x_n$ , represents the additional measurement error associated with a point target. This error is due to both thermal noise effects and target fluctuation effects. As with the system noise term, its mean value is also zero. For a constant target the Cramer-Rao bound on the variance of this term is

$$\sigma^2 = \frac{1.5 R^2}{\pi^2 \text{SNR}}$$

Here the resolution parameter  $R$  is  $\lambda/D$ , where  $\lambda$  is the radar wavelength and  $D$  the array diameter, for angle measurements, or  $C/2BW$ , where  $C$  is the speed of light and  $BW$  the pulse bandwidth, for range measurements.

When the target RCS is not constant but fluctuates with a probability density function  $p(\text{RCS})$ , an average Cramer-Rao bound may be computed as

$$\sigma_n^2 = \frac{1.5 R^2 N_0}{\pi^2} \frac{\int_{\tau}^{\infty} \text{RCS}^{-1} p(\text{RCS}) d\text{RCS}}{\int_{\tau}^{\infty} p(\text{RCS}) d\text{RCS}}$$

If the lower integration limit is taken as zero for the Rayleigh target model of interest, then this quantity is unbounded. In practice however one requires a detectable signal before a measurement is made. As a result, the lower limit can be set equal to a RCS threshold value of  $-N_0 \ln P_{FA}$ , where  $P_{FA}$  is the design false alarm probability. When this is done one obtains

$$\sigma_n^2 = \frac{1.5 R^2}{\pi^2 (1 + \overline{\text{SNR}})} \frac{E_1 \left[ -\ln(P_{FA}) / (1 + \overline{\text{SNR}}) \right]}{P_D \left[ -\ln(P_{FA}) / (1 + \overline{\text{SNR}}) \right]}$$

where  $E_1$  is the exponential integral and  $P_D$  is the detection probability, i.e.  $P_D = \text{EXP} \left[ \ln P_{FA} / (1 + \overline{\text{SNR}}) \right]$ . The resulting normalized measurement standard deviation is plotted in Figure 6 for  $P_{FA} = 10^{-4}$  and  $10^{-6}$ . Also plotted for comparison is the Cramer-Rao bound for a constant point target. Here it is observed that the measurement accuracy for a Rayleigh target is a factor of two poorer at a 30 db SNR.

The remaining term,  $X_t$ , represents the measurement error introduced by a non-point target and is the principal term of interest to this study.

**3.2 Theoretical Results.** In this section an analytic treatment of target noise effects on target location measurement accuracy is presented. The intent of this analysis was to develop a mathematical understanding of target noise effects upon which candidate target noise reduction techniques could be derived. While the analysis presented is for monopulse errors, analogous results may also be derived for range measurement errors. In either case a number of highly useful results were derived including:

- Expressions for the mean and variance of target noise measurement errors.
- Definition of the optimum data weighting/editing for track data smoothing in the presence of limiting target noise.

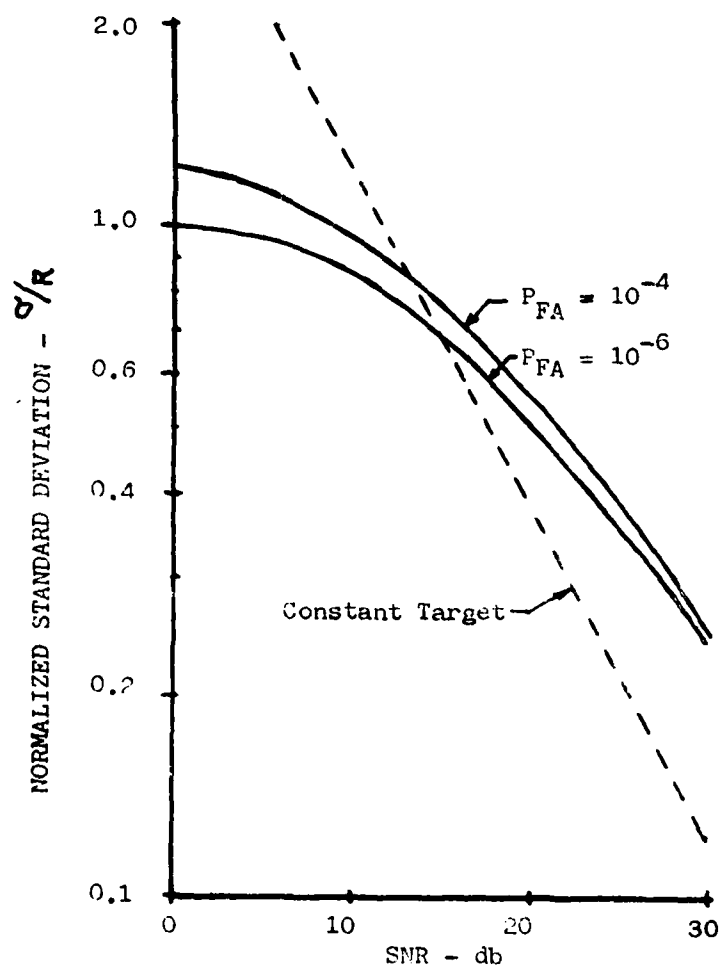


Figure 6 Rayleigh Target Measurement Standard Deviation



These results served as a basis for the target noise reduction techniques used in the simulation analysis.

3.2.1 Preliminaries. The analysis begins with the definitions of the target's angular scattering function,  $\alpha(\theta)$ , as a sample function of a zero mean circular Gaussian process over the angular width of the target, i.e.

$$\alpha(\theta) = 0 \text{ for } |\theta| > \frac{1}{2}L$$

The autocorrelation function of this process is defined by

$$E[\alpha(\theta_1)\alpha^*(\theta_2)] = S(\theta_1)\delta(\theta_1 - \theta_2)$$

i.e., the process is white in angle with expected power density in angle given by  $S(\theta)$ .

Modeling the two-way voltage response of a pair of squinted amplitude monopulse beams as  $F_{\pm} = a \pm b\theta$ , the target returns may be expressed as

$$r_{\pm} = \int_{-\frac{1}{2}L}^{\frac{1}{2}L} \alpha(\theta)(a \pm b\theta) d\theta + n_{\pm}$$

Here the receiver noise contributions  $n_{\pm}$  are zero mean, uncorrelated circular Gaussian processes with spectral density  $N_0/2$ . Since  $\alpha(\theta)$  and  $n_{\pm}$  are both Gaussian, the returns  $r_{\pm}$  and any linear combination of them are also Gaussian. When the angle between the squinted monopulse beams is equal to the 3 db beam width,  $\theta_{BW}$ , then  $a = \sqrt{2}/2$  and  $b = 1.17/\theta_{BW}$ .

Defining the monopulse sum and difference channels as sums of Gaussians

$$\Sigma = (r_+ + r_-)/2a$$

$$\Delta = (r_+ - r_-)2/b$$

which must also be gaussian with their probability density function given as\*:

$$p(\Sigma, \Delta) = (2\pi)^{-2} |\Lambda|^{-1} \exp(-\frac{1}{2}(\Sigma^* \Delta^*) \Lambda^{-1} \begin{pmatrix} \Sigma \\ \Delta \end{pmatrix})$$

---

\* H.L. Van Trees, "Detection, Estimation, and Modulation Theory" Part III John Wiley & Sons, Inc., 1971, Page 600.

where

$$\Lambda = \frac{1}{2} \begin{pmatrix} \mu_z & \rho \\ \rho & \mu_\Delta \end{pmatrix}$$

and

$$\begin{aligned} \mu_z &= E\{|\Sigma|^2\} = \int S(\theta) d\theta + N_0/2a^2 \\ \rho &= E\{\Sigma\Delta^*\} = \int \theta S(\theta) d\theta \\ \mu_\Delta &= E\{|\Delta|^2\} = \int \theta^2 S(\theta) d\theta + N_0/2b^2 \end{aligned}$$

As a result the statistics of the sum and difference channel are completely determined by the noise level and the first three moments of the target's angular RCS function  $S(\theta)$ .

Before continuing it will be useful to define two key parameters. The first is the quantity,  $m$ , defined as

$$m = \frac{\rho}{\mu_z}$$

At high signal-to-noise ratios this quantity approaches the target's angular RCS centroid location. The second parameter of interest is defined by  $w$  where

$$w^2 = \frac{\mu_\Delta}{\mu_z} - \left[ \frac{\rho}{\mu_z} \right]^2$$

This quantity is seen to approach the 2<sup>nd</sup> central moment of the target's angular RCS function at high SNR and hence is a measure of the angular width of the target.

With these definitions and knowledge of  $p(\Sigma, \Delta)$  a number of useful

expressions pertaining to monopulse errors can be derived. Defining the complex monopulse estimate as

$$Z = \frac{\sum \Delta^*}{\sum \Delta^*} = X + jY$$

where

$$X = \text{Re} [Z] = \text{monopulse signal about boresite}$$

$$Y = \text{Im} [Z] = \text{quadrature monopulse signal about boresite}$$

and

$$U = X - m = \text{monopulse signal about the angular location } m$$

one finds (see Appendix A.3)

$$p(U, Y) = \frac{W^2}{\pi [U^2 + Y^2 + W^2]^2}$$

$$p(U) = \frac{W^2}{2 [U^2 + W^2]^{1.5}}$$

$$p(Y) = \frac{W^2}{2 [Y^2 + W^2]^{1.5}}$$

These probability density functions indicate that the statistics of both U and Y depend only on the parameter W and not the target location. Further it is shown in the Appendix that:

$$E(U) = E(X) - m = 0$$

$$E(Y) = 0$$

In other words the expected value of the monopulse estimate x is the location m.

3.2.2 Variance Expressions For Data Editing & Smoothing. Techniques for combining several target position measurements in a manner which minimizes the target positional variance are of great interest. Generally two distinct classes of techniques can be defined. The first are data editing schemes which "edit out" or reject some raw measurements prior to

track smoothing. These techniques are suited to track smoothing algorithms which treat all input data equally. The second class of techniques are those which are designed to work with tracking filters which permit input data weighting. Naturally these techniques should be capable of near optimum performance.

Consider first a technique for data editing. As formulated in the previous section, the variances of both the real and quadrature monopulse components are equal and unbounded. Finite values for the variance can be obtained by treating the subset of target measurements associated with detectable signal levels. Since this is what any radar really implements, such a constraint is realistic. The statistics of the monopulse estimate  $U$  conditioned on a received signal strength of  $\alpha = |\Sigma|^2$  is Gaussian, i.e.

$$p(U|\alpha) = \frac{1}{2\sqrt{(\frac{1}{2}W^2\mu_z/\alpha)}} \text{EXP}\left\{-\frac{1}{2} \frac{U^2}{\frac{1}{2}W^2\mu_z/\alpha}\right\}$$

The variance of  $U$  conditioned on  $\alpha$  is then

$$\sigma_{U|\alpha}^2 = \frac{1}{2}W^2 \frac{\mu_z}{\alpha}$$

Here it is seen that this conditional variance is proportional to the square of the parameter  $W$  and inversely proportional to the received signal strength  $\alpha$ . As a result large glint variances are associated with small signal levels. Assuming the receiver has a signal detection threshold of  $\alpha_T$ , one can compute the average glint variance associated with detected signals as

$$\sigma_U^2(\alpha_T) = \frac{\int_{\alpha_T}^{\infty} \sigma_{U|\alpha}^2 p(\alpha) d\alpha}{\int_{\alpha_T}^{\infty} p(\alpha) d\alpha} = \frac{1}{2} W^2 \text{EXP}\left[\frac{\alpha_T}{\mu_z}\right] E_1\left[\frac{\alpha_T}{\mu_z}\right]$$

where

$$p(\alpha) = \frac{1}{\mu_z} \text{EXP}(-\alpha/\mu_z) \quad (\text{This follows since } |\Sigma| \text{ is Rayleigh})$$

and  $E_1$  is the exponential integral. Figure 7 depicts the dependence of this expression on  $x = \alpha_T/\mu_z$ . Usually the threshold  $\alpha_T$  is set to yield a given false alarm rate, i.e.  $\alpha_T = -N_0 \ln(P_{FA})$ . In this case  $x$  becomes equal to  $-\ln(P_{FA})/(1 + \text{SNR})$ . For  $P_{FA} = 10^{-6}$  and  $\text{SNR} = 25$  db,  $x$  becomes equal to .0436 and  $\sigma^2/W^2$  is found equal to 2.7.

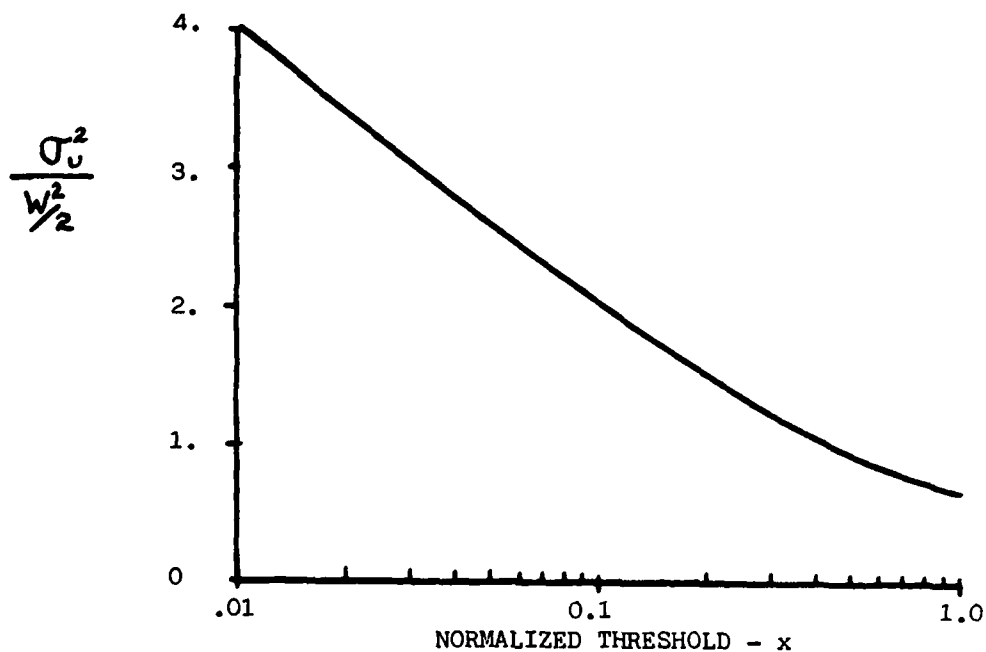


Figure 7 GLINT VARIANCE FOR DETECTED SIGNALS

Defining  $w_0$  as the limiting value of  $w$  as  $\text{SNR} \rightarrow \infty$ , one may approximate (see Appendix A.4)  $w^2$  at high SNR for a target whose RCS centroid is on boresite as

$$w^2 = w_0^2 + \frac{.365 \phi_{BW}^2}{\text{SNR}}$$

The resulting variance expression becomes

$$\sigma_u^2 = \frac{.183 \phi_{BW}^2}{\text{SNR}} \text{EXP}(x) E_1(x) + \frac{w_0^2}{2} \text{EXP}(x) E_1(x)$$

where  $x = \alpha_T/\mu_z$ . The first term represents the average Cramer-Rao bound for a Rayleigh point target. This term was discussed in Section 3.1 and plotted in Figure 6. The second term in the above variance expression represents the impact of a finite target extent. The parameter  $W_0$  is the second central moment of the target's angular RCS function and hence is a measure of the target extent. For example if the target RCS was uniform across a target extent  $\phi_w$ , then  $W_0$  would be equal to  $\phi_w/\sqrt{12}$ . For illustrative purposes, Figure 8 shows the dependence of this combined monopulse standard deviation vs SNR for  $W_0/\phi_{BW} = 0, .025, .05, .075, .1$  and a  $P_{FA}$  OF  $10^{-6}$ . For comparison the Cramer-Rao bound for a constant target is also presented. This is the value which is usually used to predict radar measurement performance.

Now assume one has a sequence of M independent monopulse estimates, each of which passed a detection threshold. One standard method of combining such data is to simply form an unweighted average, i.e.

$$\hat{U}_{AVG} = \frac{1}{N} \sum_{i=1}^N U_i$$

The resulting variance is then

$$\sigma_{AVG}^2 = \frac{1}{N} \frac{W^2}{2} \text{EXP}[\alpha_T/\mu_z] E_1[\alpha_T/\mu_z]$$

The reference\* contains a reprint of an IEEE paper which concludes on the basis of simulation that a superior technique is to select only that monopulse estimate associated with the largest signal strength. For the Rayleigh model assumed in this section it was possible to derive an expression for this referenced technique, namely

$$\sigma_{SLA}^2 = \frac{1}{2} W^2 \sum_{k=0}^{N-1} (-1)^{N-1-k} \frac{N!}{k!(N-1-k)!} \text{EXP}[(N-k)\alpha_T/\mu_z] E_1[(N-k)\alpha_T/\mu_z]$$

These two methods are compared in Figure 9 for a threshold value

---

\* "Radars, Vol.6, Frequency Agility and Diversity." edited by David K. Barton, Artech Publishers, Also see: J.M. Loomis and E.R. Graf, "Frequency-Agile Processing to Reduce Radar Glint Pointing Error," IEEE Transactions on Aerospace & Electronic Systems, November 1974.

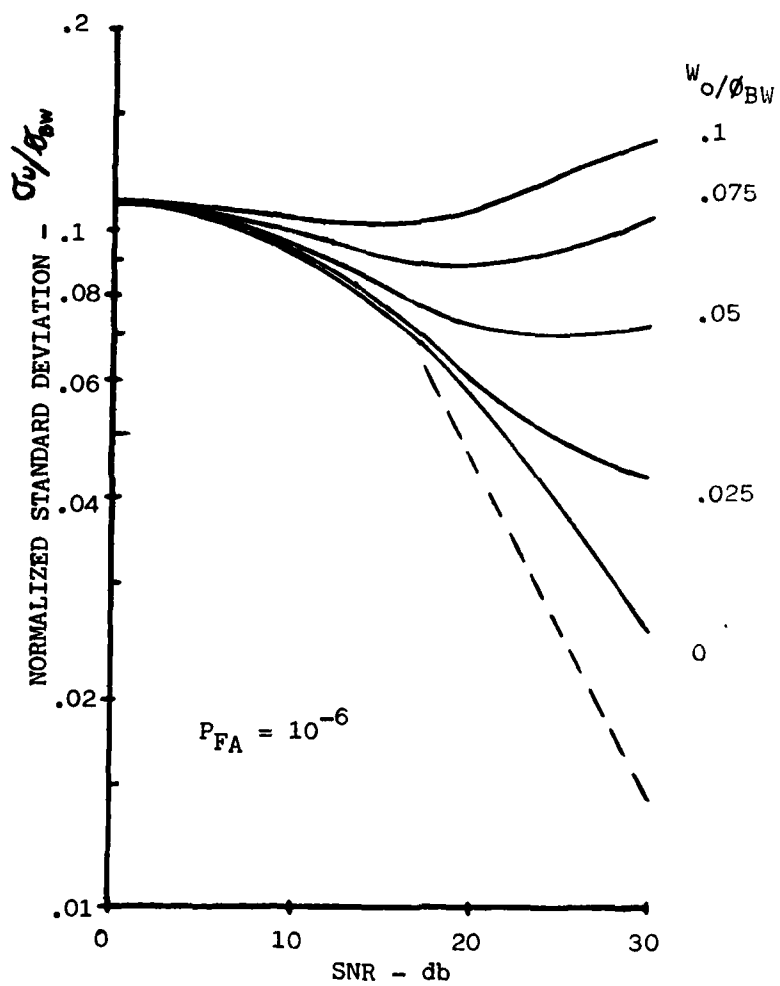


Figure 8 EFFECTS OF TARGET EXTENT AND SNR

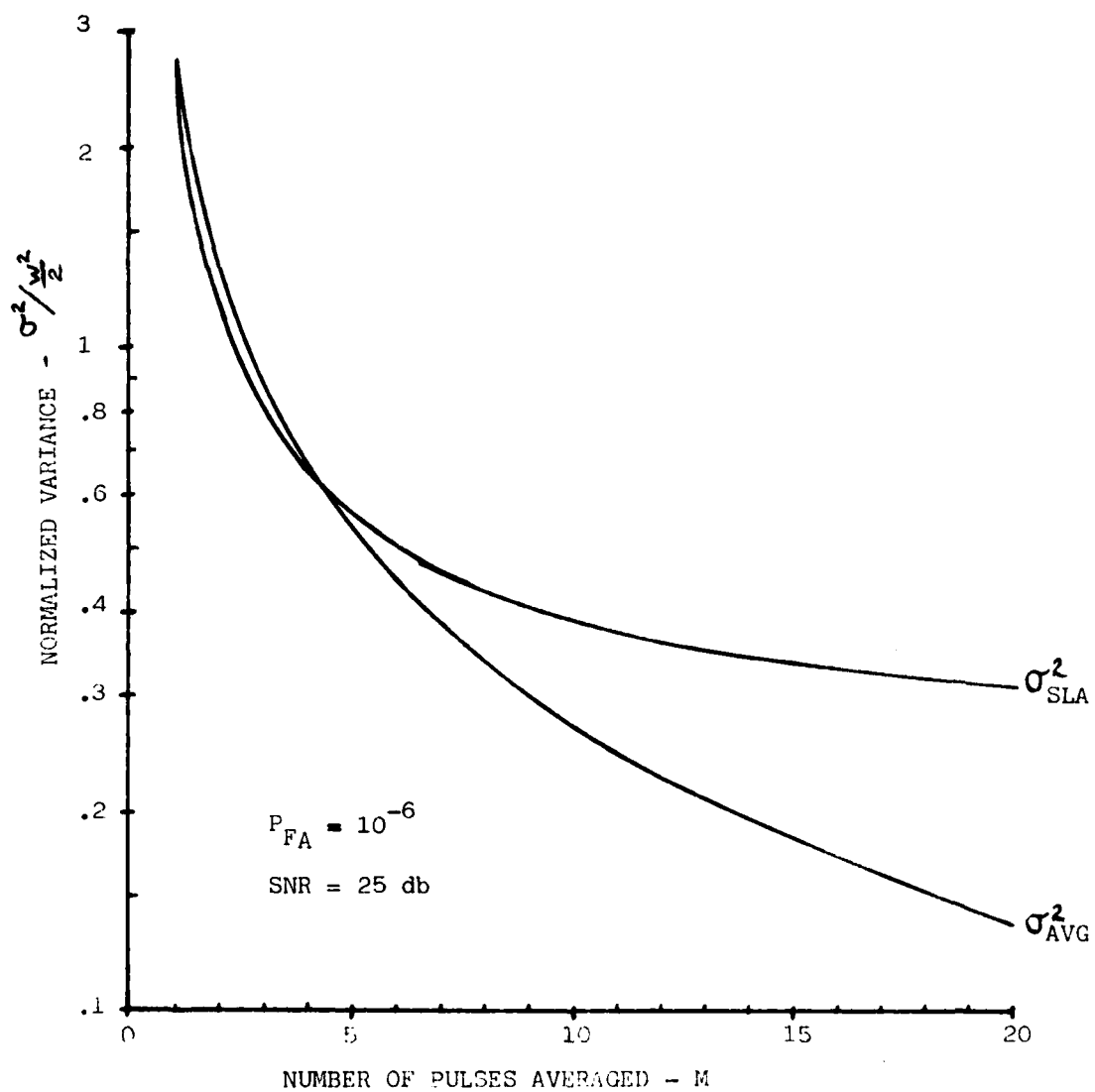


Figure 9 EFFECTS OF TWO AVERAGING TECHNIQUES



corresponding to  $P_{FA} = 10^{-6}$  and  $SNR = 25$  db, i.e.  $\alpha_T/\mu_s \approx -\ln(P_{FA})/SNR = .043$ . When the number of measurements  $N$  is between 2 and 4, the Select Largest Amplitude (SLA) technique is slightly better than an unweighted mean average. For  $N \geq 5$  however, the SLA technique becomes increasingly poorer than the mean average. As a result computing a mean average is indeed a reasonable technique.

By increasing the threshold value beyond the detection threshold, the variance  $\sigma^2(\alpha_T/\mu_s)$  can be made smaller as indicated in Figure 7. In doing so however, the signal detection probability,  $P_D = \text{EXP}(-\alpha_T/\mu_s)$ , is also reduced. In certain situations it is possible to define near optimum values for  $\alpha_T$ . Consider the tracking example in which one is concerned with the variance associated with the smoothed target position,  $\sigma_R^2$ . When the target motion can be described by a polynomial of degree  $K$ , it is well known that the target position variance approaches

$$\sigma_R^2 \Rightarrow c_K \frac{\sigma_o^2}{M}$$

where

$$c_K = \begin{cases} 1 & \text{for } K = 0 \\ 4 & \text{for } K = 1 \\ 9/4 & \text{for } K = 2 \end{cases}$$

$M =$  Total number of independent measurements.

$\sigma_o^2 =$  Constant measurement variance

To study the effects of threshold setting on  $\sigma_R^2$ , it will be assumed that the tracking filter being utilized does not permit input data weighting, i.e. all measurements are treated equally, and target noise effects dominate the measurement error. A binary weighting will be permitted in which the data is not passed to the tracking filter if the received signal is below

a given threshold value. If the measurement variance is treated as a constant, i.e.  $\sigma_o^2 = \sigma_o^2(\alpha_T)$ , and the expected number of accepted measurements taken as  $MP_D(\alpha_T)$ , then one obtains

$$\begin{aligned}\sigma_R^2(\alpha_T) &\approx C_K \frac{\sigma_o^2(\alpha_T)}{M P_D(\alpha_T)} \\ &\approx C_K \frac{\frac{1}{2}w^2}{M} \left\{ \text{EXP}(2 \alpha_T/\mu_z) E_1(\alpha_T/\mu_z) \right\}\end{aligned}$$

The term in  $\{ \}$  is plotted in Figure 10, and is found to have a minimum value of  $\approx 1.5$  when  $\alpha_T/\mu_z = .6$ . This yields a minimum value for  $\sigma_R^2$  of

$$\left\{ \sigma_R^2(\alpha_T) \right\}_{\text{MIN}} \approx 1.5 C_K \frac{w^2}{2M}$$

and a probability of accepting a measurement of  $P_D(.6) = \approx .55$ .

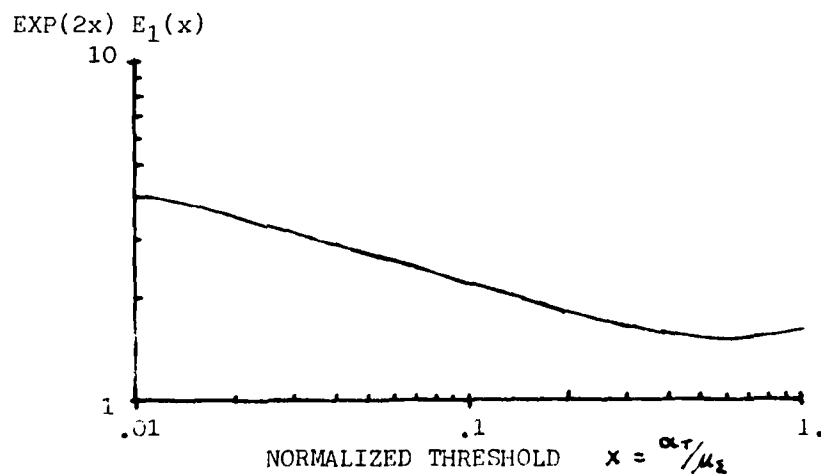


Figure 10 THRESHOLD EFFECTS ON SMOOTHED POSITION VARIANCE

At this point it is natural to ask whether thresholding some variable other than the received signal strength would yield a better binary weighting for track variance reduction. In an attempt to answer this question, the utility of thresholding the quadrature monopulse signal,  $Y$ , was also investigated. Here the conditional monopulse variance was found to be

$$\sigma_{U|Y}^2 = Y^2 + W^2 \quad (\text{See Appendix A.3})$$

This result states that large monopulse variances are associated with large values of  $Y$ . As a result, discarding measurements when  $Y$  exceeds some threshold,  $Y_T$  is a reasonable technique to investigate. When this was done the resulting track variance was found to be (see Appendix A.3)

$$\sigma_{R(Y_T)}^2 = C_K \frac{W^2/2}{M} \left\{ 2 \left[ 1 + (W/Y_T)^2 \right] \ln \left[ Y_T/W + \sqrt{1 + (Y_T/W)^2} \right] \right\}$$

The term in  $\{ \}$  was found to have a minimum value of 3.43 for  $Y_T/W = 1.3$ . For this situation 75% of the measurements are accepted and the minimum track variance becomes

$$\left[ \sigma_{R(Y_T)}^2 \right]_{\text{MIN}} = 3.4 C_K \frac{W^2}{2M}$$

Comparing this result with that obtained for thresholding the received signal strength, i.e.  $1.5 C_K \frac{W^2}{2M}$ , clearly indicates that editing on signal strength is superior.

Now consider the class of smoothing techniques which permit variable weighting of the radar measurements. For Rayleigh target, a high SNR solution for the maximum likelihood estimate of the target's RCS centroid was found to be

$$\hat{x}_{ML} = \frac{\sum_{n=1}^N \alpha_n x_n}{\sum_{n=1}^N \alpha_n} \quad (\text{See Appendix A.5})$$

That in the target position estimates,  $X_n$ , should be weighted by the associated received signal strength,  $\alpha_n = |\sum_n|^2$ . The variance of this estimator was determined (see Appendix A.5) to be

$$\sigma_{ML}^2 = \frac{1}{2}W^2/(N-1)$$

Comparing this result with those for the unweighted average and the SLA technique depicted in Figure 9, the RCS weighting is seen to be superior for  $N > 1$ . (Note the apparent discrepancy at  $N=1$  arises because no detection thresholding was assumed in the RCS weighting development).

It was also possible to derive the Cramer-Rao bound on the monopulse variance. This bound was derived and is given by:

$$\sigma_{CR}^2 = \frac{1}{2}W^2/N$$

The performance of the RCS weighting technique is seen to approach the Cramer-Rao bound for large  $N$ .

As a result, tracking filters which can weight the input measurements should use a weighting which is proportional to the received signal power.

3.2.3 Adaptive Frequency Selection. From the basic formulation for radar glint, as discussed above, it is clear that the amount of glint is inversely proportional to the radar cross section (RCS) of the scatterer. Thus, when the scattering centers on the target are in phase, yielding a maximum radar return, the radar balance point is within the physical bounds of the target, whereas when the scattering centers are out of phase, yielding a minimum radar return, the radar balance point can be far outside the physical bounds of the target. When the target is large relative to the wavelength, the relative phasing of the scattering centers can change even with small changes in target orientation, so the amount of glint can depend upon precise target orientation. Small changes in radar frequency can

affect the relative phasing of the returns from the various scattering centers, thus affecting the amount of glint.

Because of the frequency dependence of the relative phasing of scattering-center returns, it would appear to be possible to maintain a maximum RCS, and thus a minimum glint, through adaptive modification of the radar frequency. This possibility has been recognized for a long time; in fact it appears in one of the first papers devoted to the analysis of radar glint.\* A review of much of the later literature on radar glint indicates that little attention seems to have been paid this possible approach, although a great deal of effort has been devoted to techniques involving random frequency variation (or nonrandom variation over ranges large enough to assure decorrelation of the radar returns) with subsequent averaging, thresholding, filtering, etc. In the remainder of this section the problem inherent in adaptive frequency selection, a problem that has probably rendered attempts at developing such systems futile, is discussed.

In principle, it would seem reasonable to vary frequency on a pulse-to-pulse basis until a relatively large RCS is obtained. (Note that a truly maximum RCS is not really needed--what is important is to avoid nulls in RCS that lead to very large glint values.) Once a large RCS is obtained, the frequency is changed in small steps, of the order of 1 to 4 MHz for typical target sizes, with the direction of change being determined by whether the RCS is increasing or decreasing. Thus if a change by 1 MHz (e.g.) in the increasing-frequency direction leads to an increase in RCS, then the frequency is increased by 1 MHz on the next pulse. If the RCS decreases, the frequency is reduced by 2 MHz on the next pulse to compensate for having gone the wrong way with the previous pulse. This form of adaptive frequency selection, a simple hill-climbing technique, should permit one to remain near the peak RCS, thus reducing the amount of radar glint. The shifting of frequency can eventually lead to the system frequency bound,

---

\* L. Peters, Jr., and F.C. Weimer, "Tracking radars for complex targets," Proc. IEE(London), vol. 110, pp. 2149-2162, December 1963.

since the radar cannot operate over an unrestricted frequency range. When such a bound is reached, the radar must again use the random-frequency approach to acquire a new peak RCS.

When an adaptive technique such as that described above is tried, it is found that the peak RCS is indeed found and tracked for a while but then seems to be lost: the system seems to track small RCS values rather than large ones. Frequent reacquisition of RCS peaks is necessary. The reason for this problem is an apparently inherent one in the behavior of RCS as a function of aspect angle and frequency. If one thinks of RCS as an elevation over a plane in which coordinates are aspect angle and radar frequency, then what one seeks is the frequency that produces a peak RCS, i.e., a maximum elevation on the surface (and hence the hill-climbing algorithm referred to above). If the maxima of this surface are ridges, then as aspect angle changes it should be possible to vary the frequency in a manner that will keep us on the ridge (assuming the PRI is short enough so the aspect-angle change is very small). If, on the other hand, the maxima are isolated peaks, then as aspect angle changes one could not remain on a peak by changing frequency in the nearly continuous manner of the hill-climbing technique described above.

To permit an assessment of the nature of the RCS surface as a function of aspect angle and frequency, a simple three-scatter target as shown in Figure 11 was chosen. The point scatterers have scattering amplitudes B, C, and D, where the scattering amplitude is the square root of RCS. The discussion is limited to two dimensions since the addition of the third dimension adds nothing to the conclusions. Initially assume scattering amplitude B = 0 so there are only two significant scattering centers. The radar cross section is given by

$$RCS = C^2 + D^2 + 2CD\cos\left[2kcc+d'\cos\theta\right]$$

where k is the wave number and the other parameters are as defined above.

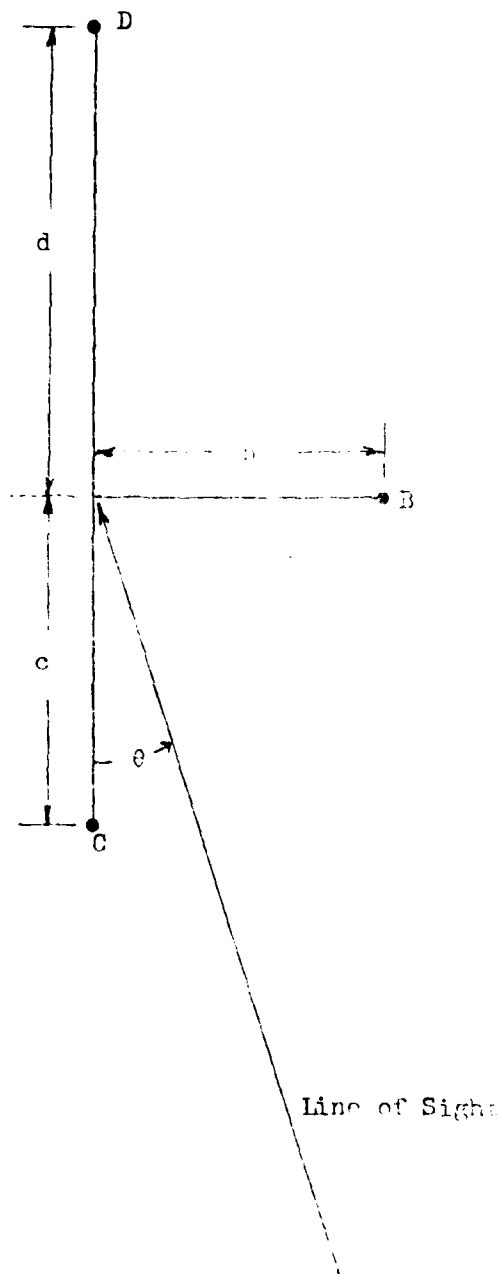


Figure 11. THREE-SCATTERER MODEL

To remain at the peak of the RCS function, it is necessary that

$$2k(c+d)\cos\theta = n2\pi$$

with  $n$  any integer. Expressing  $k$  in the form  $2\pi f/v$ , where  $f$  is the radar frequency and  $v$  is the velocity of propagation (used here because  $c$  is a length), one can show that the frequency necessary for peak RCS is given by

$$f_n = \frac{nv}{2(c+d)\cos\theta}$$

There are  $n$  possible frequencies because of the multiple peaks of the cosine function. For  $c+d = 5$  meters, the values of  $f_n$  for selected values of  $n$  are shown in Figure 12. For a given value of  $n$  the variation in  $f$  necessary to stay on this ridge of the function can vary widely unless the aspect angle is restricted to lie in a narrow band. If a frequency limit of the system is reached, it is necessary to shift to another ridge of the RCS function, i.e., to a different value of  $n$ . Still, for the 2-scatterer case it seems feasible to remain on such a ridge with only periodic shifts to new values of  $n$ .

It is obvious from the result given above that the intuitive hill-climbing idea for frequency adaptation should be practical for the two-scatterer target. Practical targets often consist of more than two scattering centers, and it is necessary to examine the behavior of the RCS contour for such targets. Now consider the 3-scatterer configuration shown in Figure 11 with  $B$  made nonzero. The RCS is given by

$$\begin{aligned} \text{RCS} = & B^2 + C^2 + D^2 + 2BC\cos[2k(ccos\theta - bsin\theta)] + \\ & 2BD\cos[2k(dcos\theta + bsin\theta)] + 2CD\cos[2k(c+d)cos\theta] \end{aligned}$$

Now one has three terms involving cosine functions, and it seems clear that one can no longer remain on a peak of the overall function by varying the frequency, since there are three terms that involve the aspect angle and target dimensions in different ways. Thus one has three sets of ridge-and-valley structures that are superimposed, and the locations of peaks depend on the locations on the frequency-angle plane at which three ridges superimpose. Figure 13 shows the ridge orientations for the three-component structures.



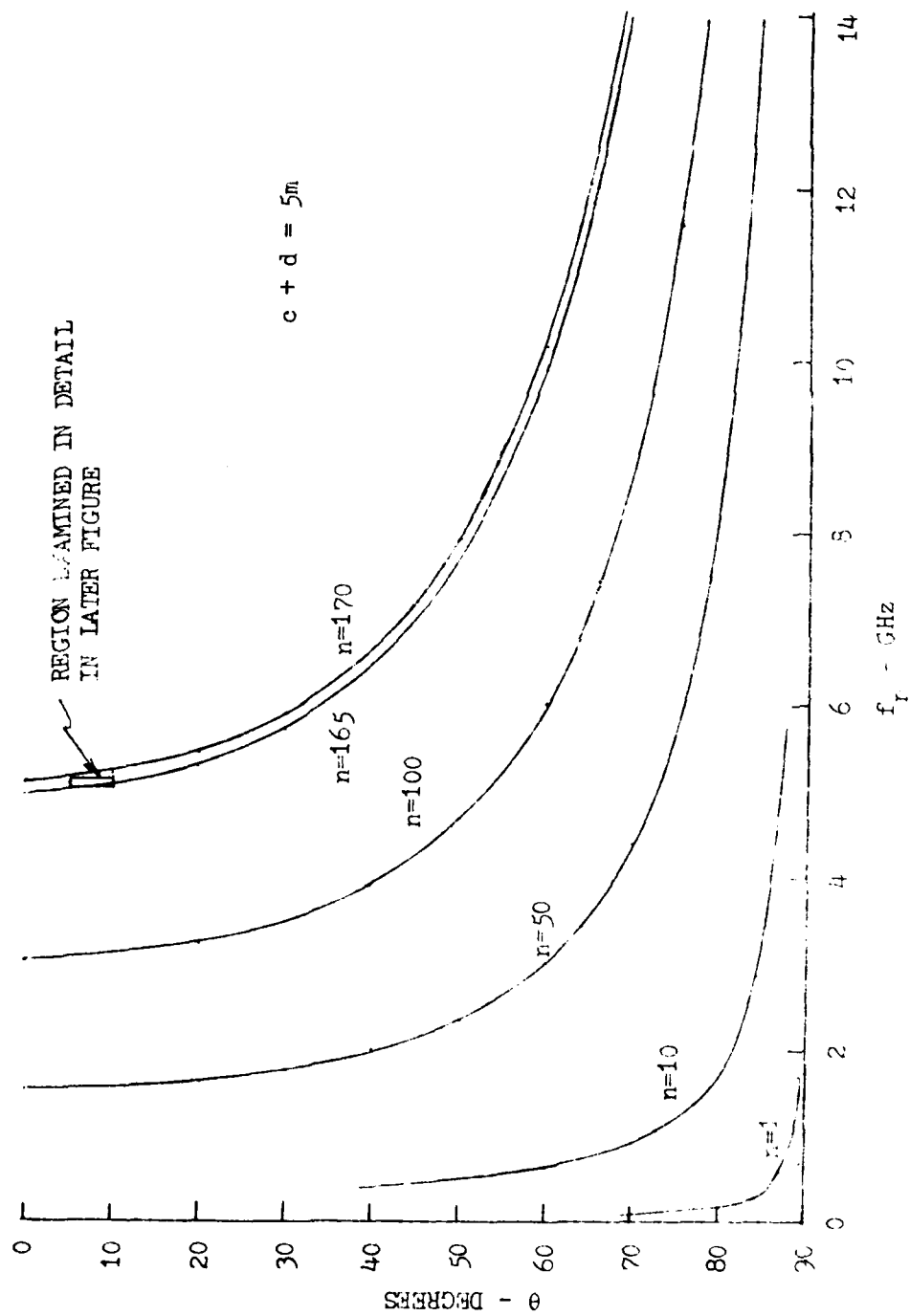


FIGURE 11. CURVES OF  $f_T$  FOR  $f_{T0}$ -SCATTERED TARGET

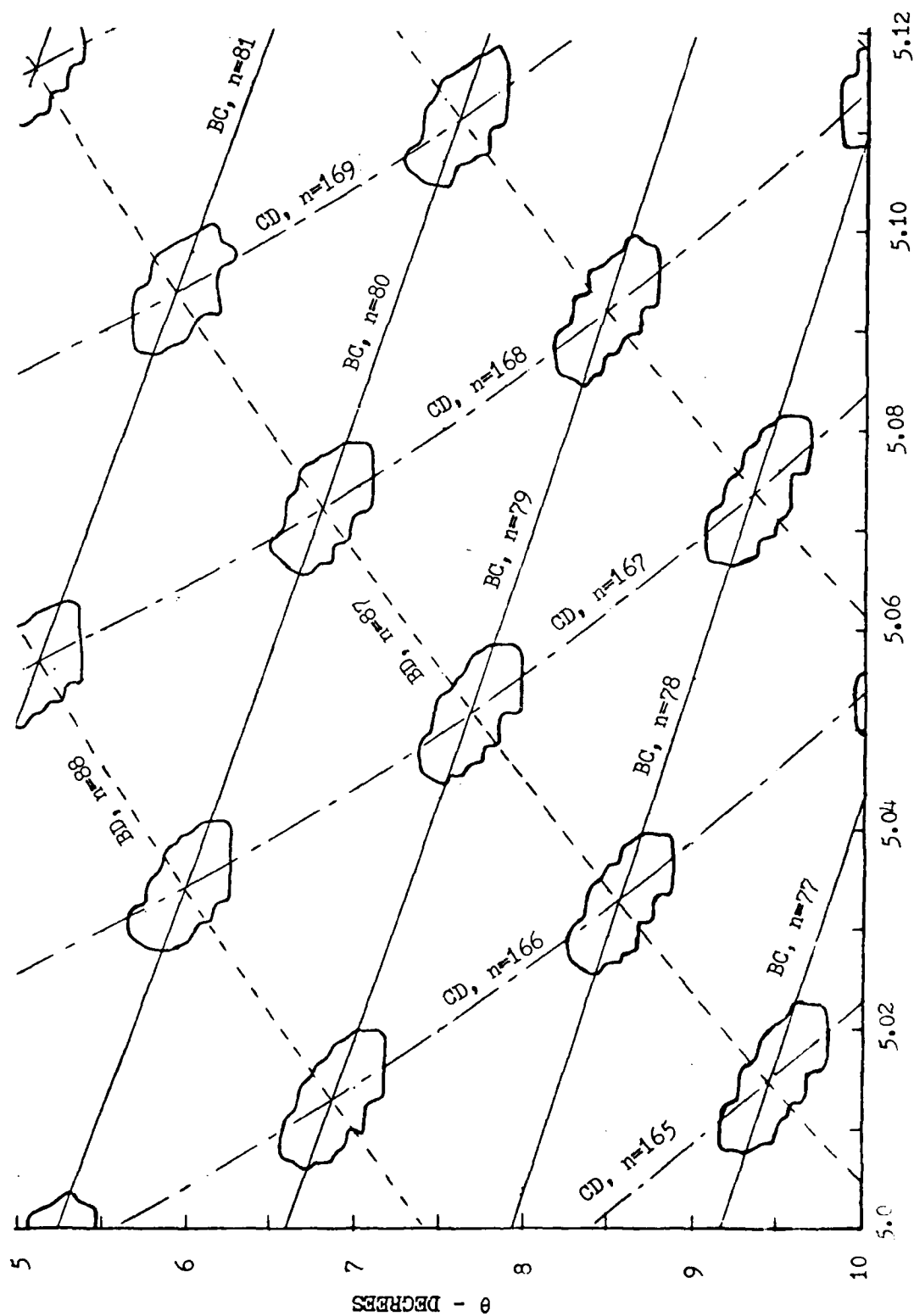


Figure 1. THREE-SCATTERER CCF SHOWING RIDGE LINES AND 80%+ PEAKS ( $b=1m$ ,  $c=d=2.5m$ )

The set of curves consisting of long and short dashes corresponds to scattering centers C and D; these lines are exactly the same ones shown on the preceding figure for the two scatterer model. The solid curves give the ridge locations for scatterers B and C, and the dashed curves, the ridge locations for scatterers B and D. Where the ridges coincide, one would expect to obtain peaks of the RCS function. For the set of scattering amplitudes  $B = 1$ ,  $C = 2$ ,  $D = 1$ , shown on this figure are approximate contours within which the RCS is 80% or more of its maximum value.

In the figure above all of the ridges lines intersected at common points, thus producing relatively symmetrical peaks. This intersection of the sets of ridges is a result of assuming  $c = d$ . If  $c$  and  $d$  are not assumed equal, a less symmetric set of peaks occur and a more complicated surface results. Similar, more-complicated surfaces will also result when more than three scattering centers contribute.

When the presence of a third scattering center produces isolated peaks rather than continuous ridges, one can see that the peak-finding (or hill-climbing) technique has very limited applicability. If the aspect angle changes by enough to take us off a local peak, the adaptive method can get trapped in a low-RCS region for many pulses. It will, in such cases, give significantly poorer performance than a random-frequency technique that uses thresholding or filtering. The only way the adaptive approach can be valid is if it incorporates a means of recognizing the locations of peaks and switching to a random-frequency tactic when a peak is left, thus seeking a new peak.

### 3.3 Simulation Results

3.3.1 Target Scattering Models. To permit numerical evaluation of radar glint and glint-reduction techniques, two target scattering models were developed. The first model was for an F-15 fighter aircraft. Detailed dimensions were not available, so figures from Janes' were used in conjunction with measurements made on a 1/72 scale model (Revell kit). The second scattering model was for a cruise missile. Here even less detailed information was available and dimensions were based upon what information could be gleaned from Janes' and from photographs in Aviation Week & Space Technology articles; the Tomahawk was chosen since more information seemed to be available for it.

For both cases, assumptions were made to permit reasonably simple radar scattering analysis to be used. These assumptions included:

- Short radar wavelengths, corresponding to frequencies above 3 GHz,
- Monostatic radar operation,
- Aspect angles limited to range of  $\pm 30^\circ$  in elevation and  $\pm 50^\circ$  in azimuth,
- Single scattering is assumed, i.e., no multiple-diffraction effects are included,
- Shadowing boundaries were crudely approximated, partially to simplify the analysis and partially because detailed consideration would require inclusion of multiple-diffraction effects,
- Scattering from engine ducts was modeled in a very crude manner, partly because of inadequate knowledge of scattering processes in ducts but primarily because of a total lack of information regarding the materials and geometry of the engine ducts involved in the F-15 and the Tomahawk.

More detailed descriptions of these scattering models are contained in the following subsections.

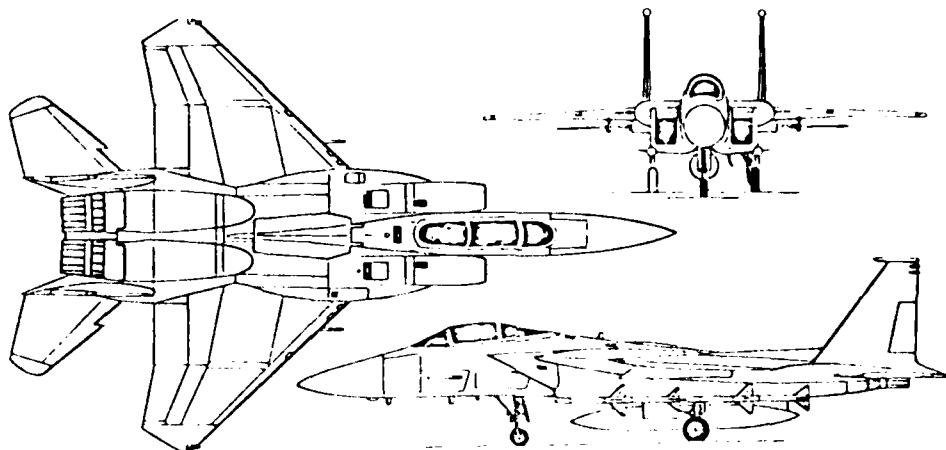
3.3.1.1 F-15 Scattering Model. An outline drawing of the F-15 and a list of its major dimensions are given in Figure 14 which has been taken from Janes'. The scattering from the aircraft was modeled by 81 scattering centers, most of them simple point scatterers used to represent scattering from the various external stores on the aircraft. Several options are available in the computer program as to which of the stores are included; if all are omitted, the aircraft itself is modeled by 31 scattering centers. A list of the scattering centers is given in Table I; some of the repetitive items are omitted.

The manner in which the scattering is approximated will not be given in detail here because of the complexity and length of discussion that would be needed. Instead, we will indicate the type of approximation that is used for each of the classes of scattering centers on the aircraft.

Edges occur at engine-duct inlets, leading and trailing edges of wing and tail surfaces, and on the missile support structure. Scattering from sharp edges is approximated through use of the geometrical theory of diffraction, which permits inclusion of polarization effects, for a two-dimensional edge in combination with a physical-optics-type approximation to account for the nonspecular incidence effects on a finite-length edge. This type of scattering approximation should be reasonably accurate for angles not too far from specular; for angles that are far from specular, the errors increase but the amount of backscatter decreases so that the errors are of less significance than would otherwise be the case.

Scattering from the scanning antenna in the nose of the F-15 was approximated by the scattering from a flat plate. Scanning of the antenna independent of aircraft motion is possible. This option has generally not been used in the computations reported here (the antenna return can be switched off for any run).

Scattering from the junction of the radome and the fuselage could not be very accurately modeled because we lacked sufficient information



DIMENSIONS, EXTERNAL:

Wing span	13.05 m
Length overall	19.43 m
Height overall	5.63 m
Tailplane span	8.61 m

Figure 14

F-15 picture from Janes'

TABLE 1

SCATTERING CENTERS ON F-15 MODEL

On Aircraft

Top edge of port engine duct intake  
Top edge of starboard engine duct intake  
Leading edge, port wing  
Leading edge, starboard wing  
Trailing edge of port wing, outer section  
Trailing edge of starboard wing, outer section  
Trailing edge of port wing, inner section  
Trailing edge of starboard wing, inner section  
Leading edge of horizontal stabilizer, inner section, port side  
Leading edge of horizontal stabilizer, inner section, starboard side  
Leading edge of horizontal stabilizer, outer section, port side  
Leading edge of horizontal stabilizer, outer section, starboard side  
Trailing edge of horizontal stabilizer, port side  
Trailing edge of horizontal stabilizer, starboard side  
Leading edge of port vertical stabilizer  
Leading edge of starboard vertical stabilizer  
Trailing edge of port vertical stabilizer  
Trailing edge of starboard vertical stabilizer  
Scanning antenna in nose of aircraft  
Junction of radome and fuselage, port side  
Junction of radome and fuselage, starboard side  
Cockpit  
Lower edge of engine duct intake, port side  
Lower edge of engine duct intake, starboard side  
Scatterer near end of port wing  
Scatterer near end of starboard wing  
Scatterer near top of port vertical stabilizer  
Scatterer near top of starboard vertical stabilizer  
Cannon at root of starboard wing  
Port engine duct

TABLE 1  
Continued

Starboard engine duct

Stores

Rear edge of port missile mount  
Rear edge of starboard missile mount  
Nose of Sparrow missile 1  
First set of fins, Sparrow missile 1  
Rear set of fins, Sparrow missile 1  
    Etc. for Sparrow missiles 2,3,4  
Nose of Sidewinder 1  
First set of fins, Sidewinder 1  
Rear set of fins, Sidewinder 1  
    Etc. for Sidewinders 2,3, 4  
Nose of bomb 1  
Tail of bomb 1  
    Etc. for bombs 2 through 12



about the aircraft. We therefore used point scatterers at the junction points as a crude, first-order approximation to the actual scattering.

Scattering from the cockpit was approximated in two ways, chosen by an input option. Either the use of a conductive canopy could be assumed, in which case there is no scattering from either the interior of the cockpit (because it is shielded) or from its exterior (because we are restricted to aspect angles for which specular reflection does not occur), or a transparent canopy could be assumed, in which case scattering from a sphere at the location of the pilot's head is assumed. Additional scattering from the interior of the cockpit also probably occurs but has not been approximated here.

Additional scattering occurs from the lower edges of the engine-duct intakes; either sharp-edge scattering or scattering from a cylinder is used to represent this scattering, depending on the elevation angle of the line of sight. Scattering from small objects at the ends of the wings and from the cannon on the starboard wing are represented by point scatterers.

As noted above, scattering from the engine-ducts, which represents a major source of scattering for angles near nose-on, could not be very accurately modeled because of a lack of detailed information regarding the ducts as well as fundamental difficulties in modeling duct scattering in any case. Basically, we assumed a fixed scattering amplitude for the duct and then used an aspect-angle-dependent factor to account for reduction in illumination as aspect angle varies. It is possible that a radar absorbing grid might be used in the duct; to allow for this case, an input parameter can be set to reduce the duct scattering by approximately 14 dB to approximate the effects of reduced duct scattering.

Scattering from the missiles and bombs that can be carried by the aircraft could be modeled using formulations for curved surfaces and ogives in combination with formulations for sharp edges such as are used for edges on the aircraft. Such modeling would also require relatively careful inclusion of shadowing effects of various stores by each other. To include all

of these effects would require a very complex computer program which would require excessive running time. Consequently, we have adopted a much simpler model: simple point scatterers are used for each set of fins on a missile or bomb and for the nose of each missile or bomb. While of limited precision, this form of approximation should be reasonable for the glint analyses of interest here.

The key characteristics of this model are presented in Figure 15. Included are forward aspect angle plots of the target's narrow band RCS and the first and second central moment of the target's RCS distribution in each of the principle measurement dimensions. These moments are of key interest because they control the mean and variance of the target noise in the corresponding radar measurement coordinates.

The data presented are for a frequency of 3 GHz. It is of interest to note that the aircraft's RCS is fairly insensitive to polarization. This is because most of the scattering arises from engine ducts which are here modeled as polarization-insensitive scatterers rather than from edges. One would generally expect polarization diversity to be ineffective as a target noise mitigation technique.

3.3.1.2 Cruise Missile Model. Figure 16 is a sketch of the simplified cruise missile configuration that was modeled. The body is essentially a cylinder 0.53m in diameter and 5.49m long. The nose is assumed to be a (conducting ellipsoid of revolution with major axis 0.96m and minor axes 0.53m. The nature of the duct interior was not know, and even the dimensions and location of the duct entrance had to be inferred from various photographs of the Tomahawk. The scattering model used here should therefore be considered as a reasonable representation of a class of missile configurations rather than as an accurate model for the Tomahawk.

The scattering centers used to represent the cruise missile are listed in Table 2. Because the wings and tail are very thin and have sharp edges, it seems reasonable to approximate the scattering from these

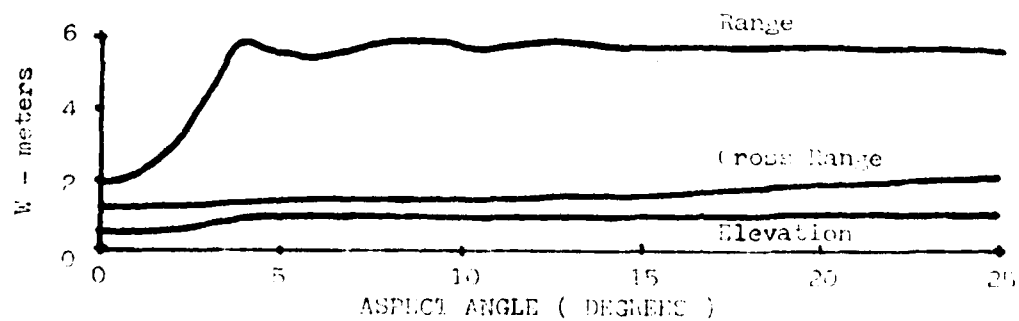
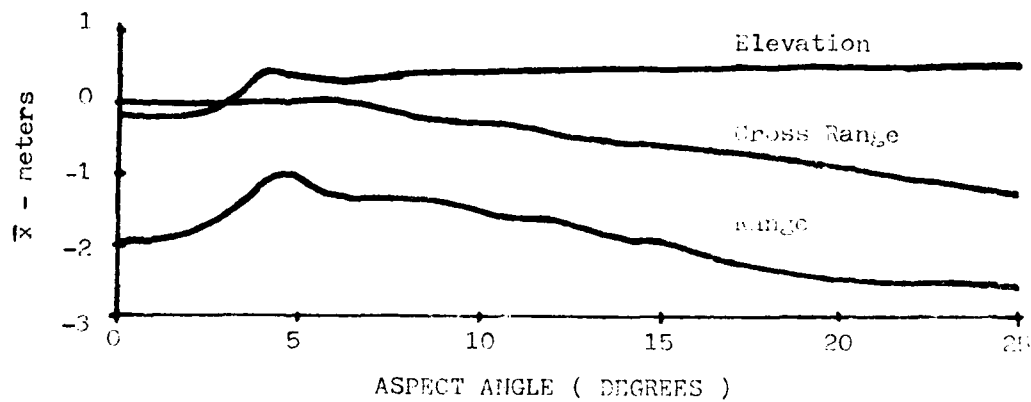
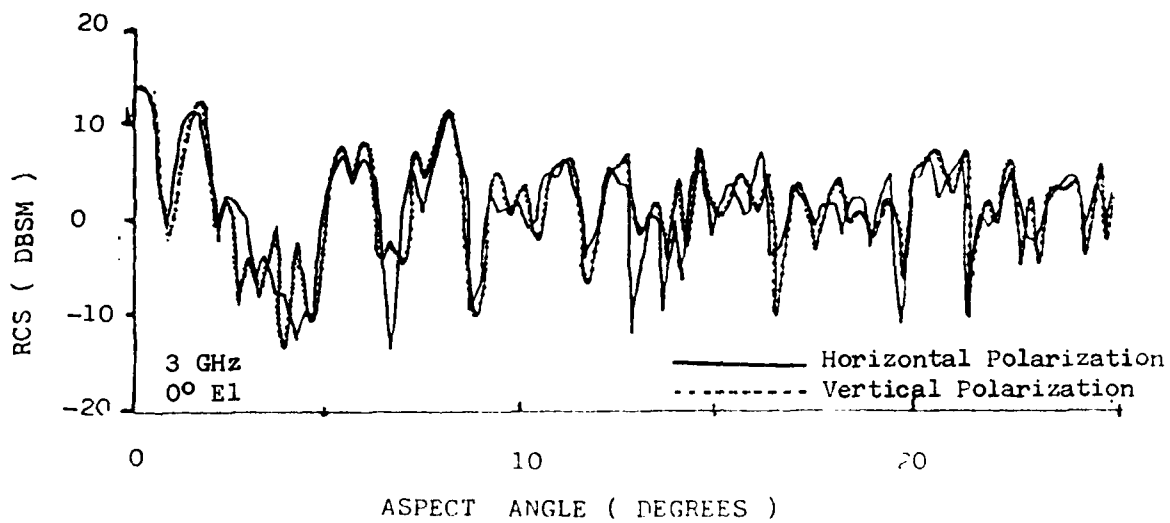
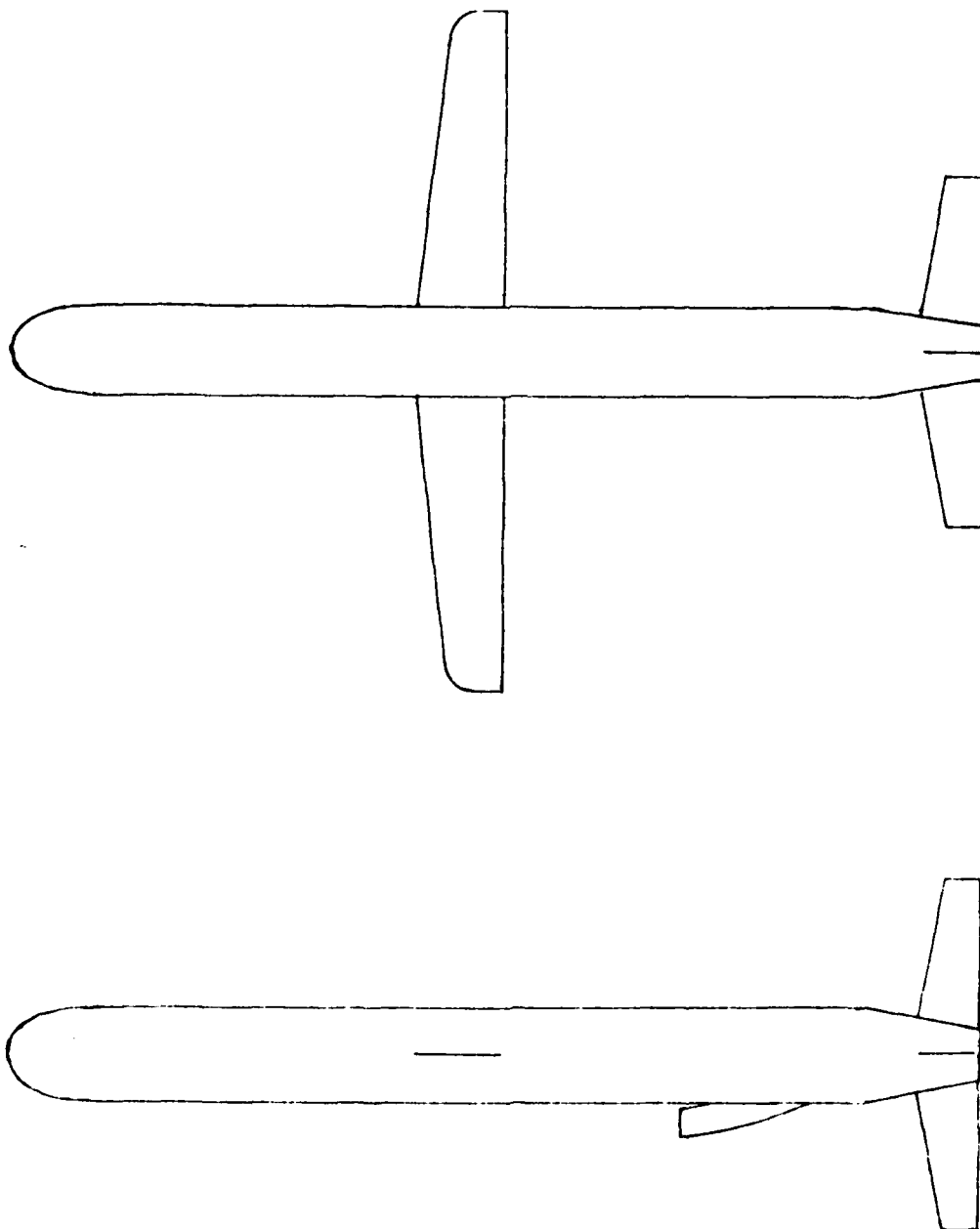


Figure 15 Key Aircraft Model Characteristics



Length = 5.49m  
Wingspan = 3.87m  
Diameter = 0.53m

Figure 16: CRUISE MISSILE USED FOR SCATTERING MODEL

edges as that from a conducting half plane. The asymptotic expression for this scattering, using the geometrical theory of diffraction, is the same as was used for the aircraft aside from the simplification here whereby the wedge angle goes to zero (i.e., the half-plane case). For the leading edges of the wings, the analysis was complicated by the presence of rounded ends. For nonspecular aspect angles, the rounded end becomes significant scattering contributor; although the scattering amplitude is relatively small, the ends of the wings are the scattering centers farthest removed laterally from the centroid of the target and thus can produce a significant contribution to the angular glint which is of primary significance here. Analysis of scattering from a straight edge with a curved end led to a complex expression involving a uniform asymptotic expansion of the scattering integral; the uniform asymptotic expansion is necessary here because the stationary-phase point of the integral approaches one of the limits of the integration.

The nose was assumed to be a conducting ellipsoid, as indicated above. We did not have information on the location of the radome, but since cruise missiles navigate by a combination of inertial navigation and radio altimeter data, it seems likely that the antenna is directed downwards and thus produces little scattering in the forward-aspect region. Therefore, we ignored the scattering from this antenna.

Scattering from the interior of the duct was treated in the same manner as the duct scattering for the aircraft: it is assumed that the scattering is reduced proportional to the intercepted area of the duct entrance. Scattering from the ring discontinuity at the duct entrance was assumed equal to the scattering from a wire ring (i.e., an RCS equal to the intercepted area of the ring) with a linear dropoff in scattering amplitude for angles off nose-on; this rate of dropoff depends on the radar wavelength, and for short wavelengths this source of scattering quickly becomes negligible.

TABLE 2

SCATTERING CENTERS ON CRUISE-MISSILE MODEL

Leading edge, port wing  
Leading edge, starboard wing  
Trailing edge, port wing  
Trailing edge, starboard wing  
Leading edge, port horizontal tail  
Leading edge, starboard horizontal tail  
Trailing edge, port horizontal tail  
Trailing edge, starboard horizontal tail  
Leading edge, upper vertical tail  
Trailing edge, upper vertical tail  
Leading edge, lower vertical tail  
Trailing edge, lower vertical tail  
Nose  
Interior of duct  
Ring discontinuity at duct entrance

Shadowing of the scatterers on the cruise-missile model is very difficult to include accurately. The problem is that most of the scatterers are edges and the illuminated portions of those edges are extended regions that are only gradually shadowed as the aspect angle (e.g.) increases. Because of other approximations that had to be made in the model, because of a lack of detailed dimensional information, as well as because of the need for a model simple enough to permit very rapid computation of scattering contributions, we adopted a very simple shadowing argument. We assume that if the aspect angle is positive, all edge scatterers on the starboard side of the missile are shadowed, and vice versa. Thus at 0 degrees aspect angle, we abruptly switch from the scatterers on one side to those on the other. A similar rule is applied for scattering from the edges on the upper and the lower tail surfaces: for negative elevation angles the lower-tail edges are seen, and for positive angles, the upper-tail edges are seen. The engine

duct is assumed to be seen for elevation angles less than  $+0.02r$  and to be shadowed for elevation angles greater than  $+0.05r$ ; a linear dropoff in scattering for angles between these values is assumed. Inclusion of the shadowing effects of the wings on the duct entrance would require very extensive computation and probably would not significantly affect the glint-analysis results in any case.

The key characteristics of this model are presented in Figures 17 and 18. Here aspect angle plots of the cruise missile's RCS, RCS centroid and 2<sup>nd</sup> central RCS moment are presented for both horizontal and vertical polarizations. Comparing the dual polarization RCS plots one notes a marked dissimilarity in behavior. This is in contrast with the aircraft results which were noted to be largely insensitive to polarization.

While the details of all these curves will not be discussed, a brief interpretation of the behavior of the cross-range RCS centroid will be presented. For these curves the missile is assumed to rotate about an axis midway between nose and tail and the centroid location is measured laterally from a line of sight passing through the axis of rotation. Thus if all of the scattering were concentrated at the axis of rotation the centroid would remain at 0.

Consider first the horizontal-polarization centroid. There is a marked trend that is followed by the centroid for most aspect angles. This trend is largely a result of the gradual motion of the duct return, although the specular return from the trailing edge of the vertical tail (which has maximum scattering for horizontal polarization) also contributes to the shift in centroid location. Actually, the return from the tail acts, in part, to offset the effect of scattering from the nose, which would in turn move the centroid towards negative values. These three principal scatterers thus produce a centroid that gradually shifts towards positive- $x$  values. There is also a large peak excursion of the centroid near 6.4 degrees. This shift is due to the specular return from the leading edge of the wing; this scatterer becomes dominant and thus shifts the centroid towards the center of

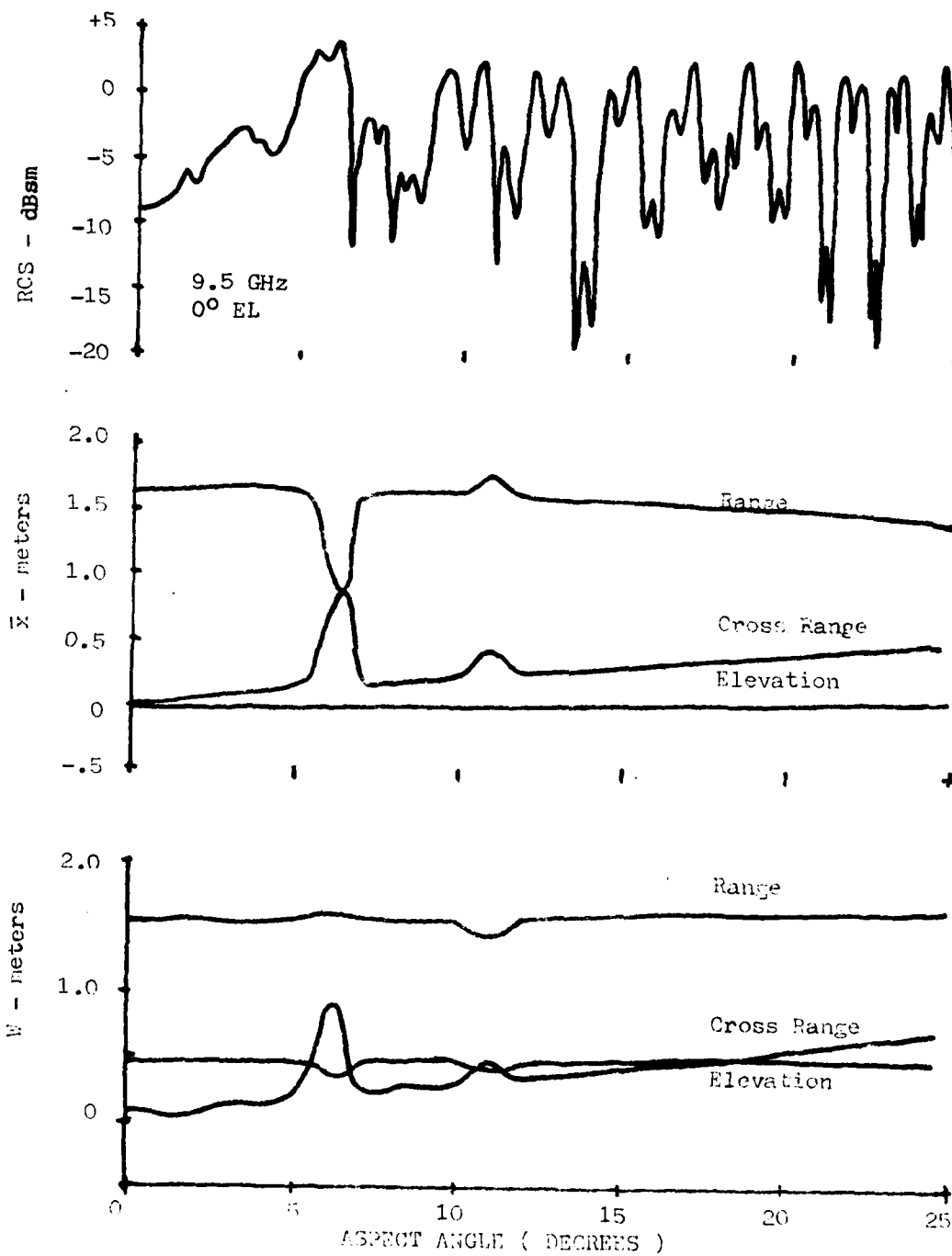


Figure 17 Cruise Missile Characteristics: Horizontal Polarization



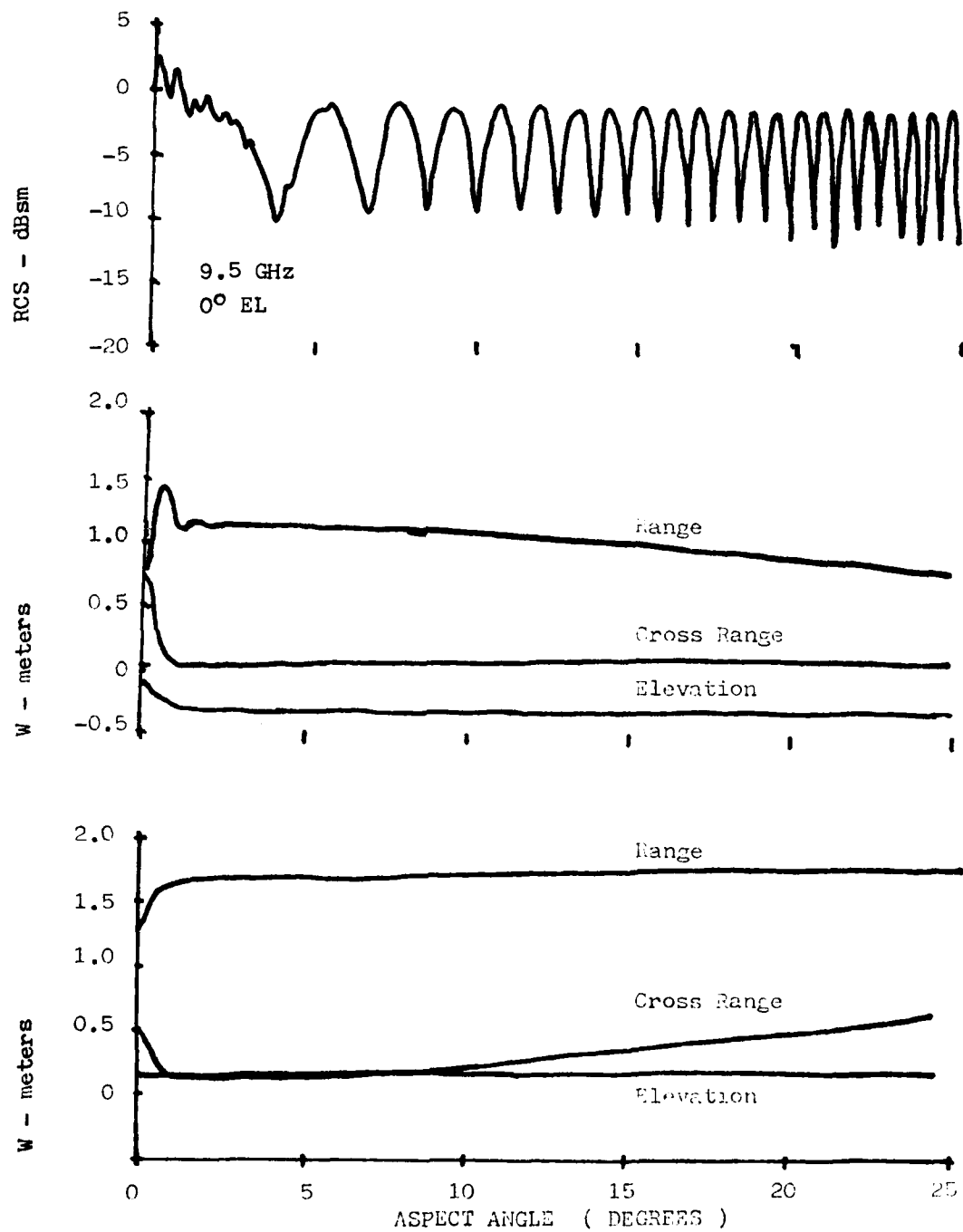


Figure 18 Cruise Missile Characteristics: Vertical Polarization

the leading edge of the wing. The smaller peak near 11 degrees is similarly produced by the leading edge of the horizontal stabilizer. As this edge is shorter, its RCS is smaller and the centroid excursion is smaller.

For vertical polarization, the leading edges of the wing and horizontal fins do not scatter, so the peaks noted in the horizontal-polarization case do not appear. Peaking of the return at 0 degrees is a result of the specular returns from trailing edges of wing and tail surfaces which are (assumed) at right angles to the axis of the missile. The trend noted before is no longer so evident, because the trailing-edge specular from the tail does not contribute here; instead, we have the nose return, which tends to move the centroid towards negative-x values, and the duct return, which tends to move it towards the positive-x values.

The behavior of the radar centroid thus seems very reasonable in terms of the scattering processes that are occurring on this body. Because of the approximations inherent in the scattering model used here, it would not be reasonable to attempt a highly detailed analysis of centroid motion. Our aim here has been to suggest that the behavior that has been observed is, in fact, consistent with the model employed.

3.3.1.3 Comparison with Rayleigh Model. Since many of the candidate target noise reduction concepts are based upon the results of theoretical analysis which assumed a Rayleigh target model, a key item of interest is to what extent do the aircraft and cruise missile models approximate a Rayleigh target. To effect such a comparison, histograms of the RCS values obtained from the aircraft and cruise missile models were compared with a Rayleigh distribution and the results presented in this section.

The aircraft RCS histograms in Figure 19 indicate that for either polarization the scattering arises from many scattering centers and therefore fits a Rayleigh distribution well.

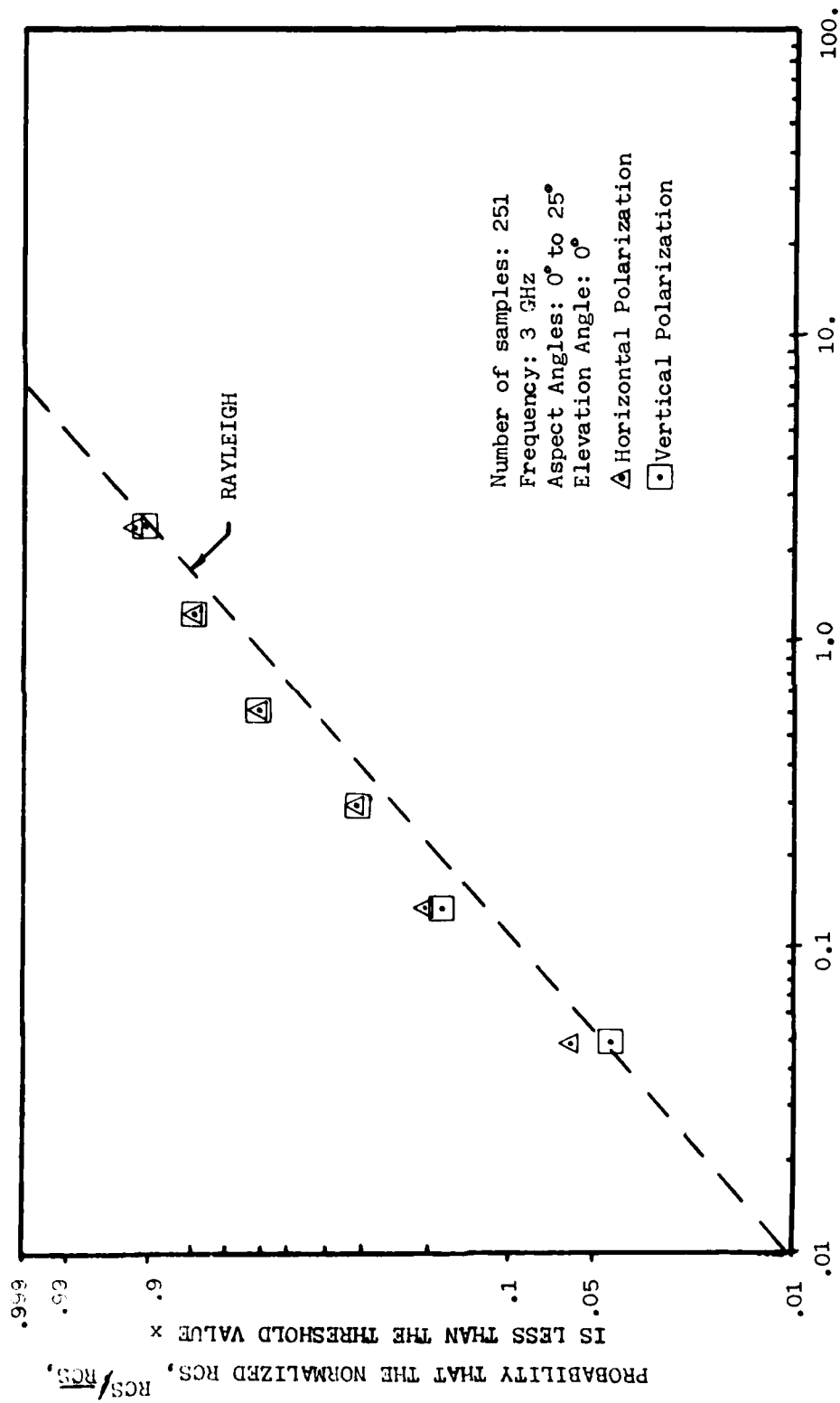


Figure 19 COMPARISON OF AIRCRAFT MODEL WITH RAYLEIGH

Unlike the aircraft model which showed little polarization dependence, the cruise missile statistics were polarization dependent. The comparisons with a Rayleigh model presented in Figure 20 illustrate this. The horizontal polarization data appear to be a reasonable fit to a Rayleigh model. The vertical polarization data, however, is not representative of a Rayleigh distribution, but closely resembles a two-scatterer distribution. Since the vertical polarization RCS is strongly dominated by the cruise missile nose and duct returns this result is not surprising.

3.3.2 Simulation Description. In section 3.3.1, the scattering models that were developed for the F-15 and the cruise missile were described. To permit estimation of glint errors and evaluation of glint-reduction techniques, it was necessary to develop a computer program that uses these scattering models. In this section the simulation program that was utilized is briefly described.

Relatively general target motions were designed into the program. The target can have pitch, roll, and yaw angles that are linearly incremented with time (only fixed-PRI cases are treated) and can have arbitrary starting points. The only restriction on these motions is that the line of sight must produce an azimuth angle within  $50^\circ$  of nose-on and an elevation angle within  $30^\circ$  of nose-on. This limitation resulted from the fact that the targets were only modeled over this region.

For any run, three frequencies are used for each aspect angle; in this way, it is possible to evaluate the effects of various frequency behaviors on glint with all other parameters held fixed. The first set of outputs is for a fixed frequency, i.e., one which is exactly the same for every pulse. The second set of outputs is for a randomly varying frequency. Here the frequency is changed from pulse to pulse on a pseudo-random basis: there is a uniform probability the frequency has any value between a specified minimum and a specified maximum frequency. The minimum and maximum frequencies need not include the fixed frequency discussed

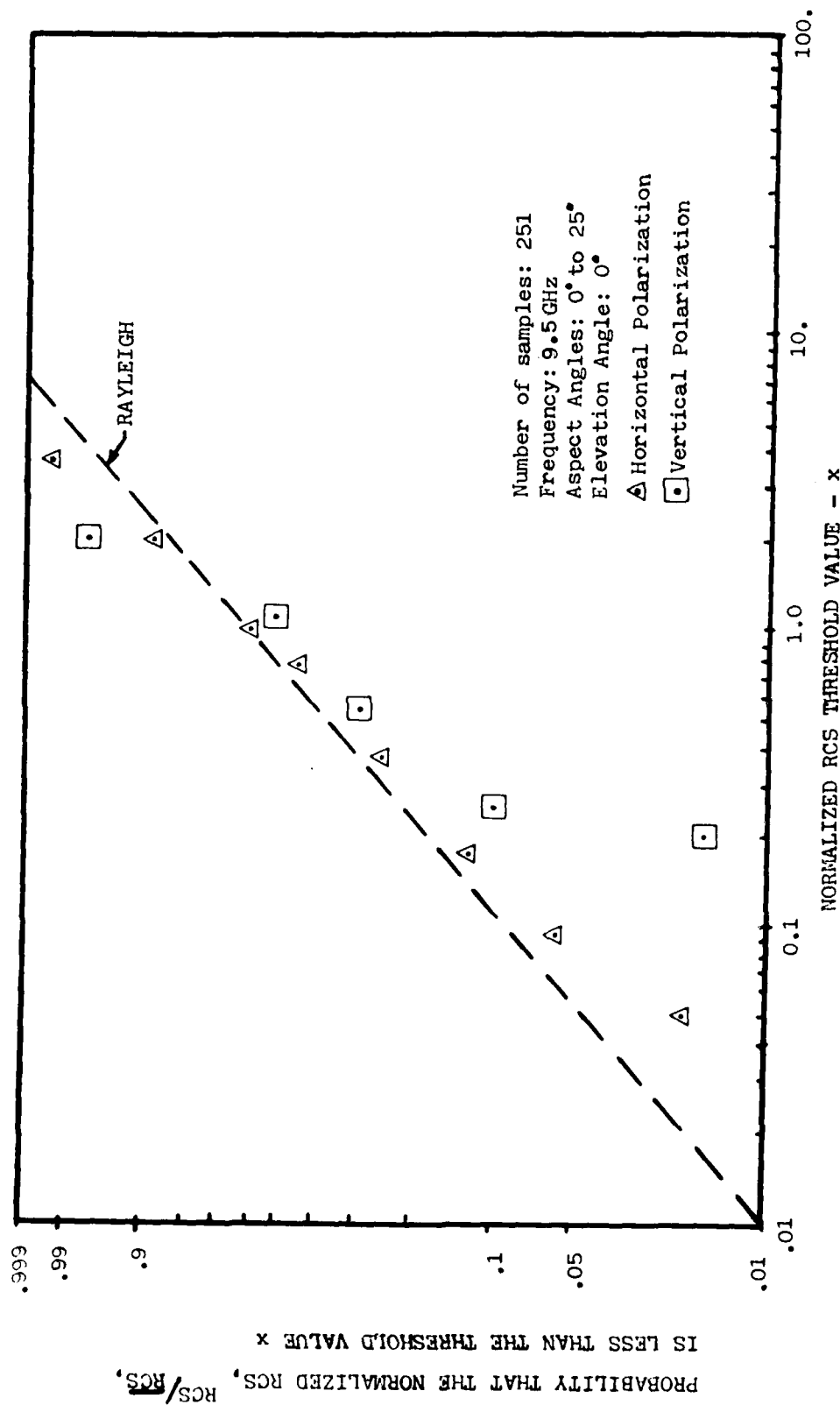


Figure 20 COMPARISON OF CRUISE MISSILE MODEL WITH RAYLEIGH

above. To make the random-frequency case more realistic, a frequency-quantization value is also assigned. For example, a frequency range from 9 to 10 GHz in 1-MHz steps may be specified. There would then be 1001 possible frequencies and they would be selected on a uniformly distributed random variable basis.

The third frequency is determined using an adaptive selection technique. Here the maximum and minimum frequencies and the frequency step are the same as were assigned for the random-frequencies case, but an attempt is made to optimize the frequency on the basis of the observed RCS of the target. Recall (Section 3.2.3) that adaptive frequency selection is expected to be difficult because of the isolated nature of the RCS peaks as a function of frequency and aspect angle. Because of limited resources and some skepticism concerning the ultimate utility of frequency adaptation, only two adaptive techniques were tested. Of these two techniques, which are described below, the second technique performed better.

The first of the adaptive frequency-selection techniques that was tried uses random frequency selection for some specified (e.g., 5) number of pulses and then chooses the frequency corresponding to the largest RCS. The frequency is then stepped (by the specified step size) and the RCS compared. If the RCS has increased, the frequency is stepped by the same amount in the same direction. If the RCS has decreased, the frequency is stepped in the opposite direction by twice the frequency-step size. This procedure continues, attempting to remain near the peak of the RCS function. As shown earlier, when there are more than two scattering centers on the target, the peaks can become isolated rather than being ridges along which a hill-climbing algorithm can be expected to maintain a high RCS value. Because the target aspect angle variations are generally not controllable, one can be forced off a peak in spite of the small-step frequency variations. To avoid this problem, whereby one could be trapped in a low-RCS region, every  $N'$ th pulse a randomly chosen frequency ( $N'$  is an input parameter of the order of 5 or 10) is used. If the RCS at the randomly chosen frequency is greater than the latest RCS obtained using the adaptive frequency selection value, the adaptive frequency

is switched so that it begins to work around a new value. In this way, if one is getting forced into a "valley" region there is a chance that a random frequency will produce an RCS nearer a peak. The main difficulty with this method is that in some cases the adaptive method gets into a "valley" region and the randomly chosen frequency also is in a low-RCS region. Many pulses may go by before one gets back to a high-RCS region. Another problem is that the use of the random frequency, when we are able to track the desired frequency adaptively, leads to a loss of usable data.

The second type of adaptive processing uses the same principle of stepping the frequency towards larger RCS values. Instead of trying a random frequency every N pulses, the adaptive method is used until the RCS falls to a level  $1/3$  that of the largest RCS to date. Actually, this largest RCS value is allowed to decay, to prevent trapping of the system by an abnormally large RCS value (e.g., a specular return only seen once), using a digital filter. If the observed RCS value is less than  $1/3$  the peak (actually, filtered-peak) value, random frequencies are used until the RCS is large enough for the adaptive processing to be resumed. In this way one avoids losing good data through a requirement to use random frequencies every N'th pulse, but now requires the use of the random-frequency method for as many pulses as necessary to get back to a peak. This second type of adaptive processing worked quite well and is used in the numerical examples presented later.

For each pulse, the orientation of the target is computed, along with the coordinate transformation matrices that are needed. The three frequencies to be used are then computed using the techniques described above. For each frequency, the RCS centroid and the second moment of the radar centroid is computed. Radar glint is found at the same time. The glint values can be found using either of two options: it can be found relative to the fixed geometrical center of the target (a point on the centerline of the target and a specified distance, usually  $\frac{1}{2}$  the length, behind the nose), or it can be found relative to the target centroid. The centroid and glint values are always found in three directions: x, z, and range. These

distances are measured relative to the radar coordinates with x a horizontal displacement, z a vertical displacement, and range measured along the line of sight, which is assumed to pass through the previously defined geometrical center of the target. In addition to the centroid and glint values, sums of these quantities and their squares (in some cases) are stored for later use in computing means and standard deviations.

An option permits printing out pulse-by-pulse data in one of two formats. In either case, the pulse number, azimuth angle, and elevation angle are printed. For each frequency the RCS is also printed. For the first option, the x, z, and range glint values are printed for each frequency; either the glint relative to the geometrical center of the target or the glint relative to the radar centroid can be printed. After the last pulse has been processed, the table concludes with the mean RCS level for each of the three frequency sets. This mean RCS is useful for evaluating the effectiveness of adaptive-frequency processing, as a highly successful adaptive choice of frequency would lead to an increased mean-RCS level.

The second option for the pulse-by-pulse table again prints aspect angle, frequency, and RCS information just as for the first option. In the x, z, and range columns, instead of glint values the locations of the centroids are printed. In a second line, below the centroids, the quantity  $(\text{second moment} - \text{centroid}^2)^{0.5}$  is printed; this quantity is a measure of the lateral (or, in the case of range, longitudinal) spread of the scattering centers on the target. The glint computations are unchanged by this choice of pulse-by-pulse output, and the subsequent summary table will be the same for this case as for the first choice of pulse-by-pulse output.

Statistical information on the target scattering characteristics is given in a table that follows the pulse-by-pulse table (when it is used). First, the program gives data relating to the radar centroid of the target. These data are given for each of the three frequency sets (i.e., fixed, randomly varied, and adaptively varied) and for each of the three coordinates



(x, z, and range). Two quantities are printed for each centroid: the mean, and the second central moment.

The remainder of the summary table contains statistics on the glint assuming various methods of processing the glint information. All of the glint values used in the statistics are computed relative to either of two references, as mentioned above, the geometrical center of the target, which remains fixed in location, or the radar centroid, which slowly varies in position on the target as aspect angle varies. A fixed threshold level, e.g., -20 dBsm, is used for all of the glint processing. The reason for this threshold is that in practice a radar has limited sensitivity and thus does not obtain data when the target RCS is below some minimum level; for very low RCS values, the glint takes on very large values that would not be seen in practice. This fixed threshold level can be made very low if inclusion of all glint values should be desired.

Using only the fixed RCS threshold, for each frequency and for each of the three coordinates, the minimum and maximum glint values, the mean glint, and the standard deviation of the glint values are printed. These results indicate the amount of glint under the assumption that no special processing to reduce glint is performed.

Next the glint statistics for three types of weighted averages are computed. In each case a running n-point average is formed and the mean and standard deviation of the resulting averaged values are calculated. This is done in each of the three measurement coordinates for each of the three frequency selection schemes. The three weighting techniques implemented are: uniform weighting; RCS weighting which was shown in Section 3.2.2 to be optimum for Rayleigh targets; and a technique termed SLA (Selection of the Largest Amplitude) in which only the glint measurement corresponding to the largest received signal is selected. The SLA technique has been reported to be optimum under some conditions.\* For each computer run up to 5 different values of n may be specified by the user.

---

\* J.M. Loomis and E.R. Graf, "Frequency-Agile Processing to Reduce Radar Glint Pointing Error," Trans. IEEE, vol. AES-10, Nov. 1974, pp. 811-820

For situations in which a radar tracking filter is not designed to individually weight the raw radar measurements, data editing of the basis of RCS thresholding may be used to reduce glint errors. To assess the effectiveness of such techniques, as well as verifying the theoretical results of Section 3.2.2., the simulation program also computes glint statistics for 5 RCS threshold settings. As in the other cases, both the resulting mean and standard deviation are computed for each of the three measurement coordinates and each of the three frequency selection schemes. In addition statistics on the percent of the data accepted at each threshold value is recorded. This data is required to normalize the resulting statistics by the probability of accepting measurements at a given threshold level.

3.3.3 Simulation Statistics. This section contains key simulation results for the two specific target models developed and described in Section 3.3.1. Generally speaking, when several dominant scattering centers existed, the target scattering was approximately Rayleigh and all the theoretical results for a Rayleigh target developed in Sections 3.2.1 and 3.2.2 were found to apply. In these situations random frequency selection and RCS weighted averages produced the greatest reduction in target noise.

3.3.3.1 Aircraft Statistics. The simulation was used to gather aircraft target noise statistics at both horizontal and vertical polarizations at a radar frequency of approximately 3 GHz. The results for both polarizations were nearly identical so only specific results for horizontal polarization will be discussed.

For all runs a -20 dBsm "detection threshold" was employed. That is, only data associated with aircraft cross sections in excess of this value were included in the statistics. For the data presented, the mean aircraft RCS was 2.25 dBsm which resulted in a normalized threshold value (i.e., threshold value + mean RCS) of  $x = .006$ . According to the theoretical results of Section 3.2.2 the normalized single pulse target noise variance should be

$$\frac{\sigma^2}{\mu^2} = e^x E_1[x] = 4.5$$

This value is noted for reference on Figure 21 which presents the normalized target noise in the range dimension as a function of the number of pulses averaged for each of the three frequency selection schemes. In all cases RCS weighting was employed. From the curves it is evident that of the three frequency selection schemes, the fixed frequency option was noticeably the poorest. Both the random and adaptive frequency options produced results near the Cramer-Rao bound of  $1/N$ , with the random technique performing slightly better.

For random frequency selection, Figure 22 presents a comparison of averaging techniques for the same simulation run. Here uniform weighting performed the worst and RCS weighting the best. This result is not surprising since RCS weighting is optimum for a Rayleigh target and the aircraft statistics were shown to be nearly Rayleigh in Section 3.3.1.3. Similar results were also obtained in the other measurement dimensions and also for the other frequency selection schemes.

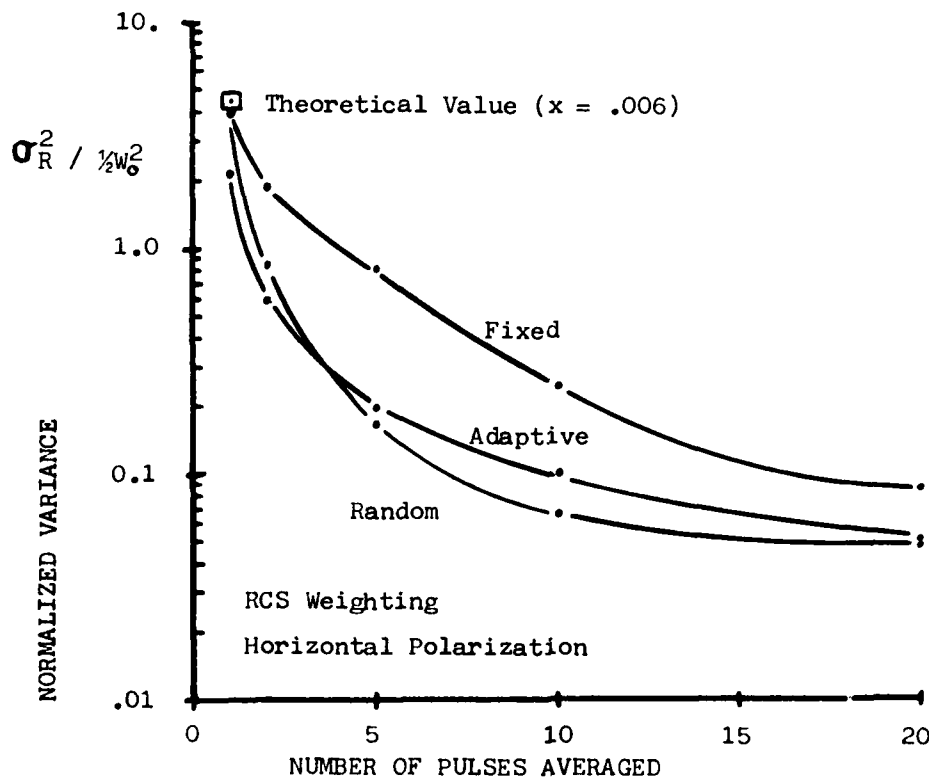


Figure 21 EFFECTS OF FREQUENCY SELECTION ON F-15 MODEL DATA

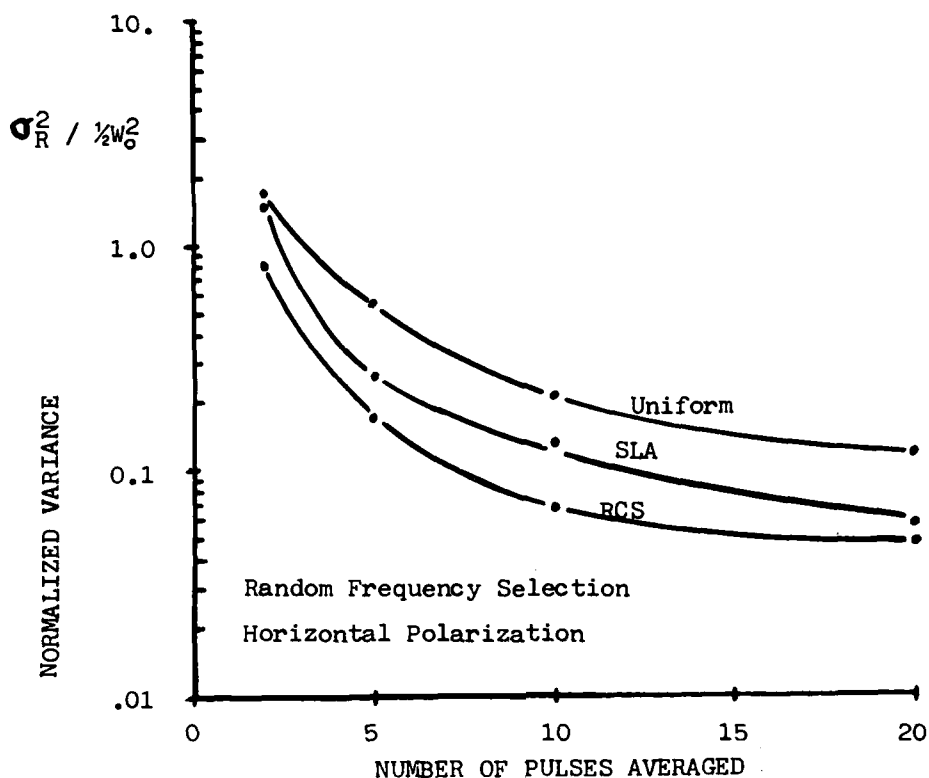


Figure 22 EFFECTS OF WEIGHTING ON F-15 MODEL DATA

Finally, results dealing with the impact of data editing on the smoothed position of a target under track are presented in Figure 23. The quantities graphed here are the normalized target noise variance  $\sigma^2 / w_0^2$  in each of the three measurement dimensions, further normalized by the  $^2$  probability of obtaining a measurement above the indicated threshold value. The rationale for this statistic comes from the fact that the smoothed target position variance varies directly with the target noise variance  $\sigma^2$ , and inversely with the expected number of measurements used in the filtering process,  $NP_D$ . Generally as the threshold value  $x$  is increased, the target noise variance is reduced but so is the number of measurements exceeding the threshold. The theoretical results of Section 3.2.2 indicated that for a Rayleigh target (see Figure 10) the statistic of interest has a minimum in the region of  $x = .6$ . The simulation results are observed to generally support this prediction. For a Rayleigh target, the probability of detection given a threshold value of  $x$  is  $\text{EXP}(-x)$ , hence for  $x = .6$  only about 55% of the raw radar measurements should be used for tracking with algorithms which do not permit input data weighting.

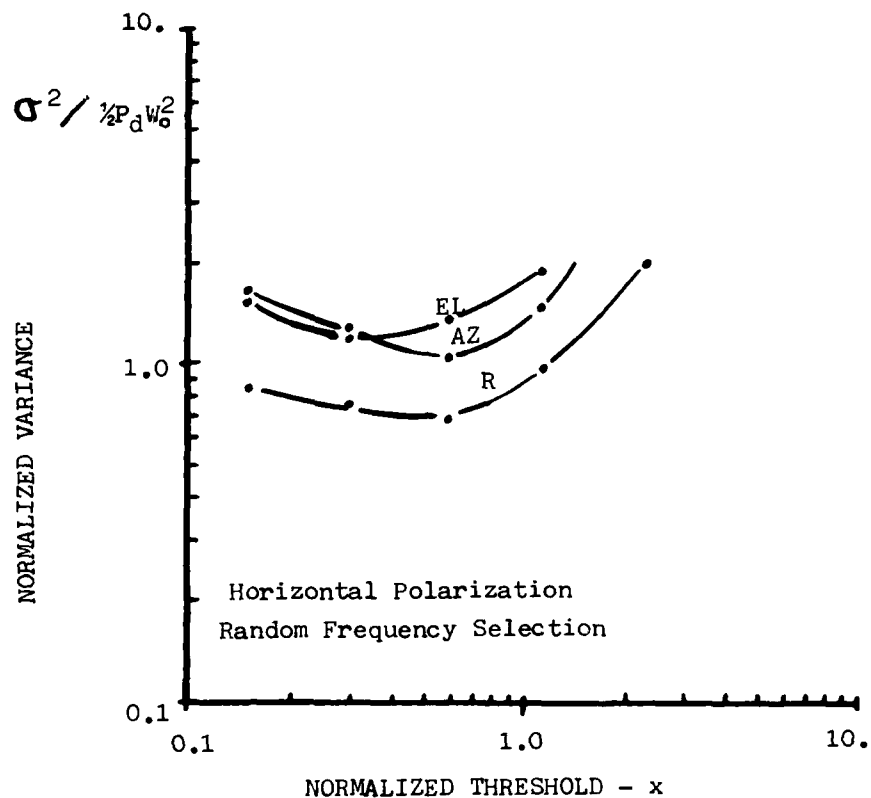


Figure 23 EFFECTS OF THRESHOLDING ON F-15 MODEL DATA

In addition to the frequency selection techniques cited above, a limited simulation analysis concerning the utility of polarization diversity was also conducted. Specifically the simulation was run for both horizontal and vertical polarization at the same frequency and the pulse-by-pulse measurements stored. In addition, a third run at horizontal polarization was made at a frequency offset by 5 MHz and the pulse-by-pulse data also stored.

With this set of data, RCS weighted-two pulse averages were computed for both dual polarization and dual frequency. The results, which are presented in Table 3, clearly indicate that dual frequency diversity was superior. This was not an unexpected result for the aircraft model because of the high degree of correlation (i.e. over 80%) between the dual polarization RCS. On the other hand the 5 MHz change in frequency was sufficient to largely decorrelate the target RCS and therefore increase the performance of the dual diversity scheme.

Table 3 Diversity Comparisons

	<u>Range</u>	<u>Azimuth</u>	<u>Elevation</u>
$\left[ \frac{\sigma_{\text{Dual Frequency}}}{\sigma_{\text{Dual Polarization}}} \right]$	.66	.70	.67

3.3.3.2 Cruise Missile Statistics. Using the cruise missile model in the simulation, analysis similar to that conducted on the aircraft model was performed, but only at a nominal frequency of 9.5 GHz. These results are highlighted in this section.

The first general result pertains to the pulse-to-pulse frequency selection procedure. As in the aircraft runs, compared were fixed frequency, adaptive frequency and random frequency selection techniques. Without exception the random frequency selection consistently provided the best performance while the fixed frequency performed the worst. Figure 24 presents a representative example of this result. Here, for horizontal polarization, the normalized target noise variances in the range dimension are compared for the three frequency selection techniques. The results for the random frequency selection are not far from the Cramer-Rao bound for Rayleigh targets.

The next result of interest pertains to the preferred weighting technique for averaging measurements. In the theoretical results of Section 3.2.2 it was shown that RCS weighting was optimum for a Rayleigh target.

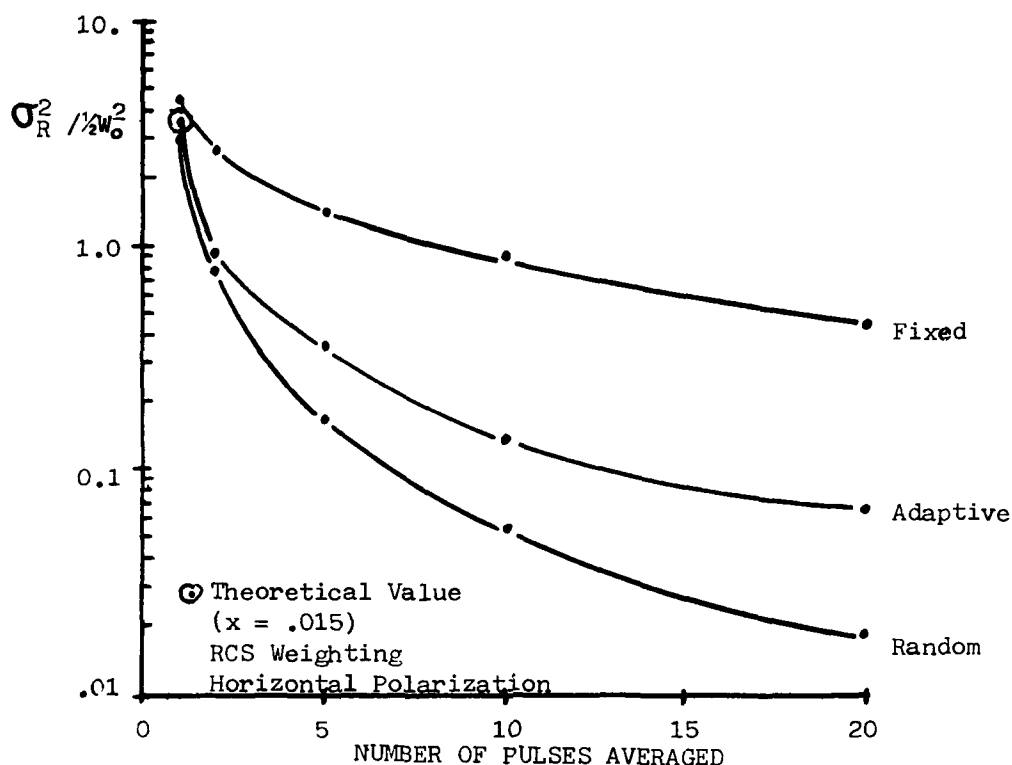


Figure 24 EFFECTS OF FREQUENCY SELECTION ON CRUISE MISSILE DATA

Section 3.3.1.3 subsequently showed the cruise missile statistics to be essentially Rayleigh for horizontal polarization but not for vertical polarization in the  $0^\circ$  elevation cut analyzed. Representative results for the cruise missile are shown in Figure 25 and 26. For horizontal polarization, RCS weighting is shown to be best, which is consistent with the Rayleigh model. For vertical polarization, however, RCS weighting did not produce the best result. Recall that for this polarization the target RCS statistics were dominated by two scattering centers, namely the missile nose and engine intake. For this case a stronger RCS weighting is evidently optimum. The selection of the measurement associated with the largest received amplitude (SLA) was previously shown to perform best on simple targets,\* and indeed it

\* J.M. Loomis and E.R. Graf, "Frequency-Agile Processing to Reduce Radar Glint pointing Error", Trans. IEEE, vol. AES-10, Nov. 1974, pp. 811-820

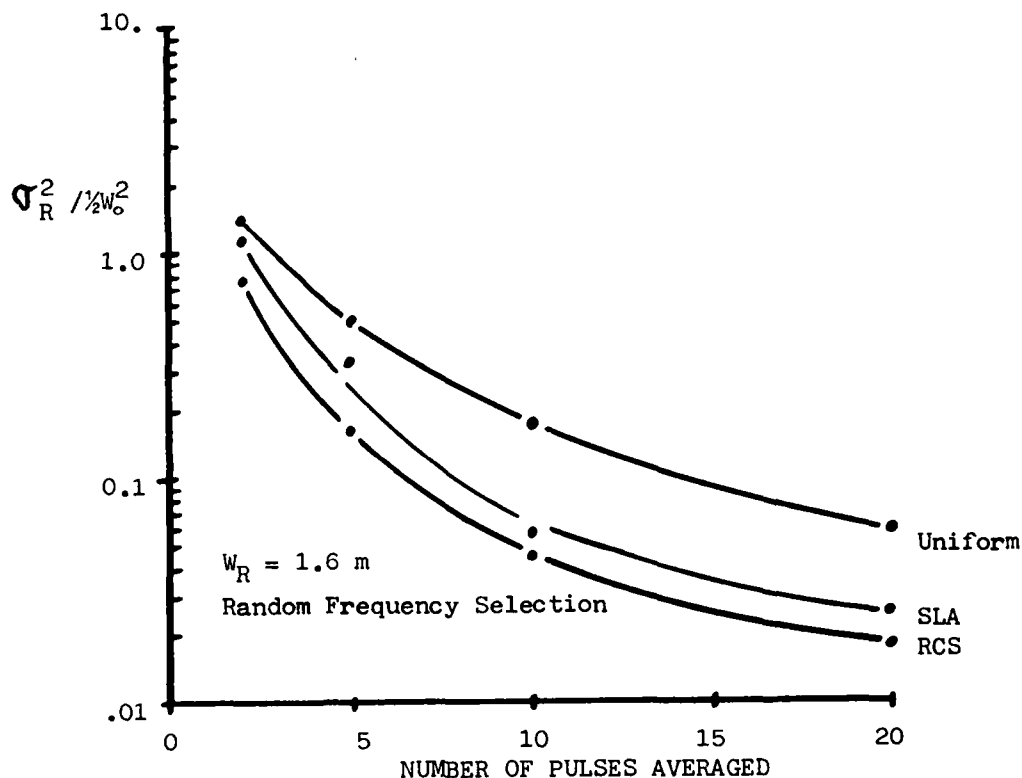


Figure 25 EFFECTS OF WEIGHTING ON HH CRUISE MISSILE DATA

was found to perform better than RCS weighting for the case at hand.

Representative results of the effects of threshold setting on data editing for tracking are presented in Figure 27. In general the best threshold setting for horizontal polarization was near the theoretical threshold value of .6 and produced a normalized variance very near the predicted value of 1.5. Since the vertical polarization case was far from a Rayleigh situation, it was not surprising that a similar optimum threshold did not exist. In keeping with the SLA finding of Figure 26, the threshold is probably the one that yields the single SLA value.



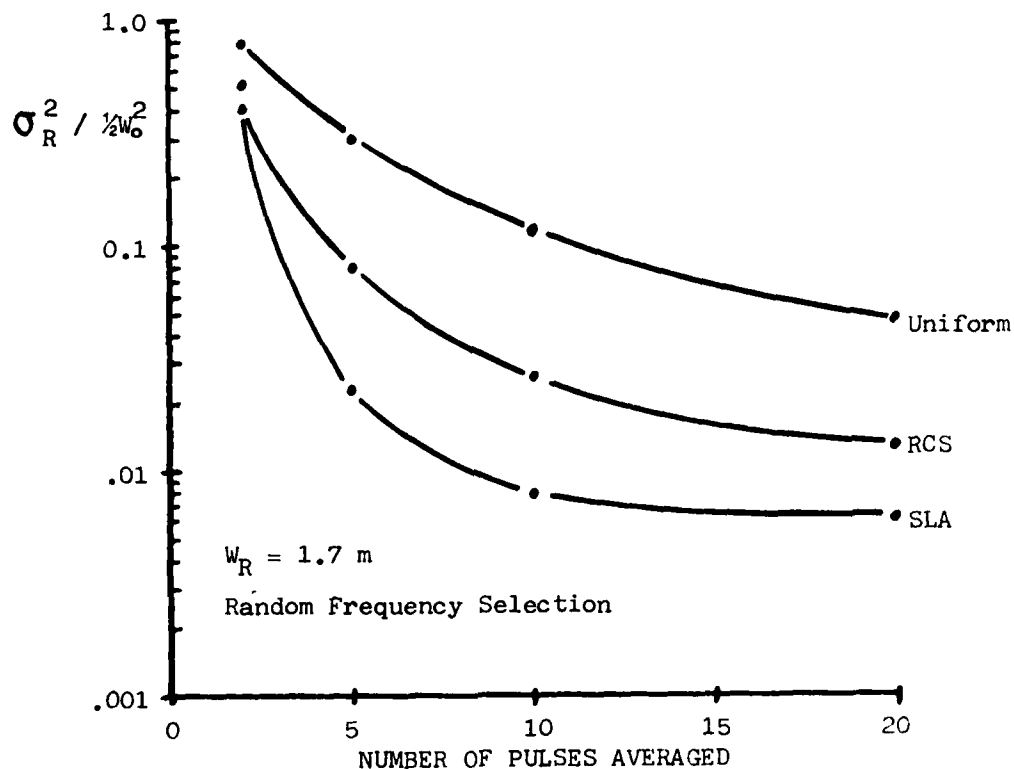


Figure 26 EFFECTS OF WEIGHTING ON VV CRUISE MISSILE DATA

The final result of interest pertains to a comparison of dual polarization and frequency diversity as a target noise reduction technique. Unlike the aircraft situation, the dual-polarization cruise-missile cross sections were not highly correlated and polarization diversity proved nearly as effective as frequency diversity.

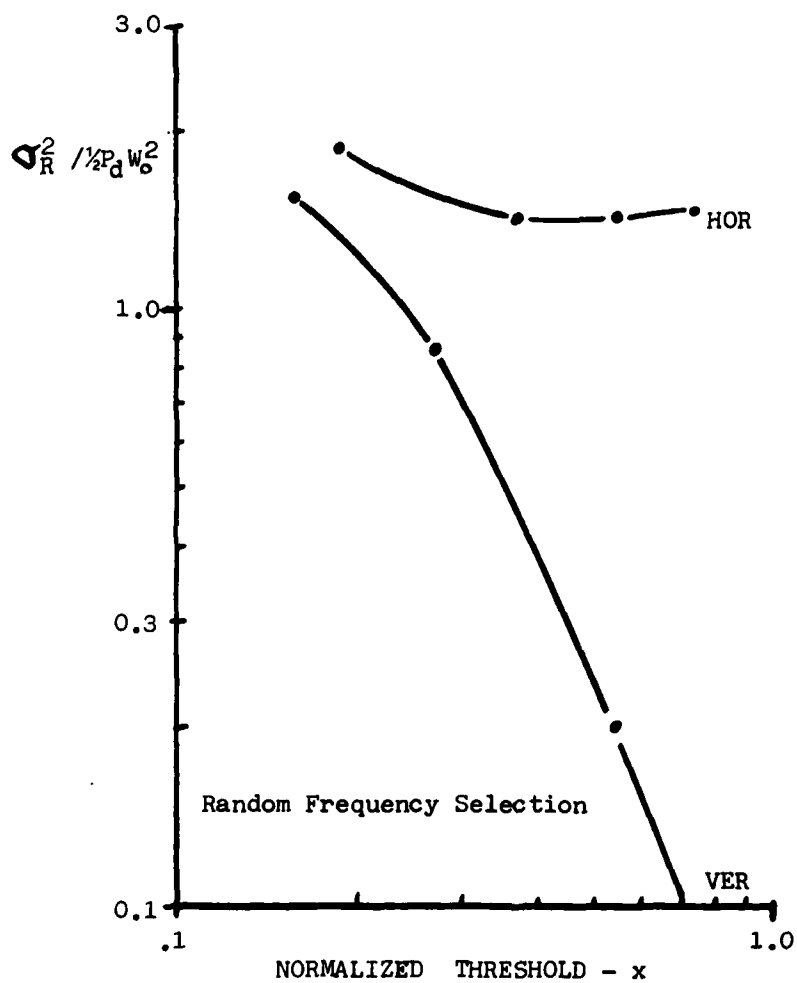


Figure 27 EFFECTS OF THRESHOLDING & POLARIZATION ON CRUISE MISSILE

3.4 Operational Implications. In general, target noise effects must be considered in the radar measurement error budget when this error component becomes comparable to the thermal noise component. In Section 3.2.2, the combined glint error variance for a Rayleigh target was shown to be approximately

$$\sigma^2 = \left[ \frac{.133 \theta_{BW}^2}{\text{SNR}} + \frac{w_o^2}{2} \right] e^x E_1[x]$$

Here the first term represents the thermal noise component, and the second term, the target noise component. Equating these two terms and graphing the resulting equality one obtains Figure 28. Here the ratio of the target's angular extent parameter  $w_o$ , normalized by the radar beamwidth is plotted vs signal-to-noise ratio. For situations above the curve, target glint effects must be considered. Completely analogous results also exist for target range noise.

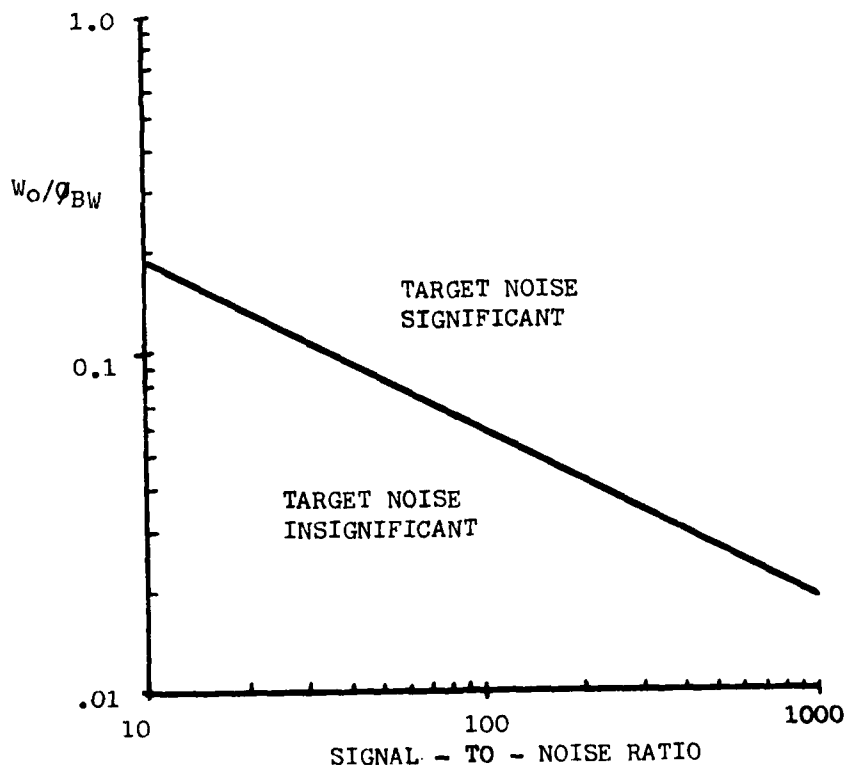


Figure 28 CONTOUR OF EQUAL THERMAL & TARGET NOISE

In terms of diversity schemes for decorrelating pulse-to-pulse target noise, frequency diversity appears to be the best choice. Generally speaking, temporal diversity doesn't produce sufficient decorrelation and depending upon the scattering characteristics of a target, polarization diversity may not be effective either. As far as frequency selection schemes go, pseudo-random frequency selection appeared to be the best all around technique.

Given the means of obtaining uncorrelated pulse-to-pulse target noise returns, the question of data editing or averaging must be considered. For complex targets such as aircraft, the target's RCS statistics can be assumed to be nearly Rayleigh, and the theoretical Rayleigh results utilized. For tracking filters which do not permit weighting of the input measurement data, a data editing scheme on the basis of the received target power was shown very effective. Here a threshold setting equal to six tenths of the average target power is recommended. The average variance of the radar measurements accepted in this manner was shown to be approximately  $.82 W_0^2/2$ , where  $W_0$  is the target extent parameter in the radar measurement dimension of interest. Since only about 55% of the available measurements are accepted by the threshold test, the resultant smoothed target position variance is proportional to  $1.5 \frac{W_0^2}{2N}$ , where  $N$  is the total number of unthresholded measurements.

For those situations in which input data weighting is permissible, weighting on the basis of the signal power was shown optimum for Rayleigh targets. This type of weighting produced "averaged" target variances near the Cramer-Rao bound of  $\frac{W_0^2}{2N}$ .

For targets whose scattering characteristics were more representative of a deterministic two scatterer target than a Rayleigh target, heavier RCS data editing and weighting is apparently optimum. In this situation better performance was obtained with the SLA technique than with RCS weighting. Effectiveness of intermediate techniques were not evaluated. As a result, while RCS weighting can still be utilized quite effectively, better techniques do exist for non-Rayleigh targets.

#### 4. KEY FINDINGS AND RECOMMENDATIONS

Addressed in this study were aspects of target noise effects as they pertain to the long range detection problem and the short range very precise track problem. By far, the major effort and most significant findings dealt with the precision track problem.

For the analytic studies in support of both of these problems, the target amplitude statistics were assumed Rayleigh. Generally 4 to 6 near equal target scatterers were found adequate for near Rayleigh statistics. A fairly detailed modeling of an F-15 aircraft also produced an essentially Rayleigh target behavior. The detection analysis performed was limited to a search radar that noncoherently integrated target returns. Generally speaking, detection performance was shown to degrade with increasing pulse-to-pulse correlation. While the general comparison between unity pulse-to-pulse correlation (Swirling I) and zero pulse-to-pulse correlation (Swirling II) is well documented the results for intermediate correlation values are believed new but not profound.

Several new and novel results were obtained, however, for the target noise problem associated with very precise radar measurements. These results pertain to the radar measurement errors of glint and the analogous range noise error. In both instances, the key target parameters of interest are the target RCS centroids  $\rho$ , in each radar measurement coordinate, and the second central RCS moments  $W_0^2$ , in these same coordinates. For high SNR conditions, the average target measurement location was shown to be the corresponding location of the target RCS centroid. The Cramer-Rao bound on the associated target noise variance was shown to be  $W_0^2/2N$ , where  $N$  is the number of independent measurements averaged. When averaging independent measurements under high SNR conditions, RCS weighting was shown to be optimal and resulted in a variance of  $W_0^2/2(N-1)$ .

Finally, in those instances in which weighting is impractical, data editing on the basis of an RCS threshold was shown to be very effective in reducing target noise variances. A threshold of six tenths of the mean target RCS was shown to be optimum.

In general all these Rayleigh results were supported via simulation analyses using the aircraft model. Similar results for a cruise missile model indicate that a heavier RCS weighting is optimum for simpler non-Rayleigh targets, i.e. two point scatterers. This result was not pursued to any great extent and may warrant additional investigations in the future.

To provide uncorrelated pulse-to-pulse target noise statistics, frequency diversity was found to be preferable to both temporal and polarization diversity. Pseudo random frequency selection was shown to be more effective in reducing target noise errors than either fixed frequency techniques or a class of adaptive frequency selection techniques investigated. An analysis of the basic problem of trying to adapt the radar frequency in such a way as to maximize the target RCS and hence minimize target glint, raised serious questions as to the feasibility of such a concept.

# APPENDIX A.1 DERIVATION OF CORRELATION COEFFICIENT FOR ROTATING BODY.

In Section 2.1.2 an expression for the correlation between two returns at different frequencies was developed. A similar expression can be developed for two returns from a rotating body taken at different times. The geometry is as shown in Figure 2 with the body rotating about the origin of the Cartesian system.

With the frequency fixed, the complex narrowband return (assuming small rotations) is represented as a function of time:

$$A(t) = \text{EXP}(-j4\pi R_o f/c) \int_{-1/2 W_x}^{1/2 W_x} \int_{-1/2 W_y}^{1/2 W_y} \alpha(x,y) \text{EXP}(-j4\pi f(y+x\omega_R t)/c) dx dy$$

where  $\omega_R$  = rotation rate

$$\rho = \frac{E[A(t_1)A^*(t_2)]}{E[|A(t_1)|^2]} = \frac{\iint s(x,y) \text{EXP}(-j4\pi f\omega_R x(t_1-t_2)/c) dx dy}{\iint s(x,y) dx dy}$$

Define a normalized crossrange scattering function  $S_x(x)$  as:

$$S_x(x) = \frac{\int s(x,y) dy}{\iint s(x,y) dx dy}$$

Then the correlation function is given as:

$$\begin{aligned} \rho(\nu) &= \int S_x(x) \text{EXP}(-j2\pi \nu x) dx \\ &\approx \rho(0) - j2\pi \nu \int x S_x(x) dx - 2\pi^2 \nu^2 \int x^2 S_x(x) dx \end{aligned}$$

where the variable  $\nu = 2f\omega_R(t_1-t_2)/c$

## APPENDIX A.2 NONCOHERENT INTEGRATION OF CORRELATED GAUSSIAN (i.e. RAYLEIGH) AMPLITUDE) RETURNS.

The received data consists of  $M$  complex returns,  $z_1, z_2, \dots, z_M$ . Let the data vector  $Z_M$  represent:

$$Z_M = \begin{pmatrix} z_1 \\ z_2 \\ \vdots \\ z_M \end{pmatrix}$$

The components  $z_m$  are samples of a correlated complex gaussian process. The covariance matrix of the samples is:

$$\Lambda_M = \frac{1}{2} E [Z_M Z_M^+]$$

where the operation  $( )^+$  represents conjugate transpose.

The probability density function of receiving a specific vector,  $Z_M$ , is given by a gaussian density:

$$p(Z_M) = ( (2\pi)^M |\Lambda_M| )^{-1} \exp( -\frac{1}{2} Z_M^+ \Lambda_M^{-1} Z_M )$$

It is desired to define a test between the two hypotheses and evaluate the performance of the test.

$H_0$  = Hypothesis 0: Data is noise alone.  $\Lambda_M = \frac{1}{2} N_0 I$

$H_1$  = Hypothesis 1: Data is Rayleigh signal + noise so that

$\Lambda_M - \frac{1}{2} N_0 I$  is positive definite.

The class of tests to be evaluated is the quadratic forms in  $Z_M$ :

$$q = \frac{1}{2} Z_M^+ Q_M Z_M \underset{H_0}{\overset{H_1}{\gtrless}} \gamma$$



Performance of this test can be found if the probability density function of  $q$  can be derived. This can be accomplished by first finding its characteristic function.

$$\begin{aligned}\phi_M(\omega) &= E[e^{j\omega q}] = \iiint \dots \int \text{EXP}(\frac{1}{2} j\omega Z_M^+ Q_M Z_M) p(Z_M) dz_1 dz_2 \dots dz_M \\ &= ((2\pi)^M |\Lambda_M|)^{-1} \iiint \dots \int \text{EXP}(-\frac{1}{2} Z_M^+ (\Lambda_M^{-1} - j\omega Q_M) Z_M) dz_1 \dots dz_M \\ &= (|I - j\omega \Lambda_M Q_M|)^{-1}\end{aligned}$$

where the limits on all integrals are from  $-\infty$  to  $+\infty$ .

Let  $\Psi_M$  be a unitary transform which diagonalizes  $\Lambda_M Q_M$ ,  
i.e.  $\Psi_M^+ \Psi_M = I$  and  $\Psi_M^+ \Lambda_M Q_M \Psi_M = D_M$

$$D_M = \begin{pmatrix} \beta_1 & & 0 \\ & \beta_2 & \\ 0 & & \ddots \\ & & & \beta_M \end{pmatrix}$$

where  $\beta_m$  is the  $m$ -th eigenvalue of  $\Lambda_M Q_M$ . Note that  $|\Psi_M| = 1$  and therefore:

$$\begin{aligned}|I - j\omega \Lambda_M Q_M| &= |\Psi_M^+ (I - j\omega \Lambda_M Q_M) \Psi_M| = |I - j\omega D_M| \\ \phi_M(\omega) &= \left( \prod_{m=1}^M (1 - j\omega \beta_m) \right)^{-1} = \prod_{m=1}^M (1 - j\omega \beta_m)^{-1} \\ F_M(q) &= (2\pi)^{-1} \int_{-\infty}^{\infty} \phi_M(\omega) \text{EXP}(-j\omega q) d\omega = \text{probability density of } q. \\ &= (2\pi)^{-1} \int_{-\infty}^{\infty} \frac{\text{EXP}(-j\omega q)}{\prod_{m=1}^M (1 - j\omega \beta_m)} d\omega\end{aligned}$$

This integration can be carried out for a variety of cases. Only two cases will be shown here assuming simple noncoherent integration, i.e.

$$Q_M = I.$$

CASE 1: Distinct Eigenvalues. Signal + White Noise.

By a partial fraction expansion one obtains that:

$$\left( \prod_{m=1}^M (1 - j\omega \beta_m) \right)^{-1} = \sum_{m=1}^M \alpha_m (1 - j\omega \beta_m)^{-1}$$

where the constants  $\alpha_m = \left( \prod_{\substack{k=1 \\ k \neq m}}^M (1 - \beta_k / \beta_m) \right)^{-1}$

$$p_1(q) = (2\pi)^{-1} \sum_{m=1}^M \alpha_m \int_{-\infty}^{\infty} \frac{\text{EXP}(-j\omega q)}{(1 - j\omega \beta_m)} d\omega$$

$$= \sum_{m=1}^M \alpha_m \beta_m^{-1} \text{EXP}(-q / \beta_m) U(q)$$

where  $U(q)$  is a unit step function.

$$U(q) = \begin{cases} 0 & q < 0 \\ 1 & q \geq 0 \end{cases}$$

The probability of detection is then:

$$\Gamma_D = \int_{\gamma}^{\infty} p_1(q) dq = \sum_{m=1}^M \alpha_m \text{EXP}(-\gamma / \beta_m) \quad \gamma > 0$$

CASE 2: M Equal Eigenvalues. Noise Alone.

$$\Lambda_M = \frac{1}{2} N_0 I$$

$$Q_M = I$$

Performance of this test can be found if the probability density function of  $q$  can be derived. This can be accomplished by first finding its characteristic function.

$$\begin{aligned}\phi_M(\omega) &= E[e^{j\omega q}] = \iiint \dots \int \text{EXP}(\frac{1}{2} j\omega Z_M^+ Q_M Z_M) p(Z_M) dz_1 dz_2 \dots dz_M \\ &= ((2\pi)^M |\Lambda_M|)^{-1} \iiint \dots \int \text{EXP}(-\frac{1}{2} Z_M^+ (\Lambda_M^{-1} - j\omega Q_M) Z_M) dz_1 \dots dz_M \\ &= (|I - j\omega \Lambda_M Q_M|)^{-1}\end{aligned}$$

where the limits on all integrals are from  $-\infty$  to  $+\infty$ .

Let  $\Psi_M$  be a unitary transform which diagonalizes  $\Lambda_M Q_M$ ,  
i.e.  $\Psi_M^+ \Psi_M = I$  and  $\Psi_M^+ \Lambda_M Q_M \Psi_M = D_M$

$$D_M = \begin{pmatrix} \beta_1 & & & \\ & \beta_2 & & \\ & & \ddots & \\ & & & \beta_M \end{pmatrix}$$

where  $\beta_m$  is the  $m$ -th eigenvalue of  $\Lambda_M Q_M$ . Note that  $|\Psi_M| = 1$  and therefore:

$$\begin{aligned}|I - j\omega \Lambda_M Q_M| &= |\Psi_M^+ (I - j\omega \Lambda_M Q_M) \Psi_M| = |I - j\omega D_M| \\ \phi_M(\omega) &= \left( \prod_{m=1}^M (1 - j\omega \beta_m) \right)^{-1} \\ p_M(q) &= (2\pi)^{-1} \int_{-\infty}^{\infty} \phi_M(\omega) \text{EXP}(-j\omega q) d\omega = \text{probability density of } q. \\ &= (2\pi)^{-1} \int_{-\infty}^{\infty} \frac{\text{EXP}(-j\omega q)}{\prod_{m=1}^M (1 - j\omega \beta_m)} d\omega\end{aligned}$$

This integration can be carried out for a variety of cases. Only two cases will be shown here assuming simple noncoherent integration, i.e.

$$Q_M = I.$$

CASE 1: Distinct Eigenvalues. Signal + White Noise.

By a partial fraction expansion one obtains that:

$$\left( \prod_{m=1}^M (1 - j\omega \beta_m) \right)^{-1} = \sum_{m=1}^M \alpha_m (1 - j\omega \beta_m)^{-1}$$

$$\text{where the constants } \alpha_m = \left( \prod_{\substack{k=1 \\ k \neq m}}^M (1 - \beta_k / \beta_m) \right)^{-1}$$

$$p_1(q) = (2\pi)^{-1} \sum_{m=1}^M \alpha_m \int_{-\infty}^{\infty} \frac{\text{EXP}(-j\omega q)}{(1 - j\omega \beta_m)} d\omega$$

$$= \sum_{m=1}^M \alpha_m \beta_m^{-1} \text{EXP}(-q / \beta_m) U(q)$$

where  $U(q)$  is a unit step function.

$$U(q) = \begin{cases} 0 & q < 0 \\ 1 & q \geq 0 \end{cases}$$

The probability of detection is then:

$$P_D = \int_{\gamma}^{\infty} p_1(q) dq = \sum_{m=1}^M \alpha_m \text{EXP}(-\gamma / \beta_m) \quad \gamma > 0$$

CASE 2: M Equal Eigenvalues. Noise Alone.

$$\Lambda_M = \frac{1}{2} N_0 I$$

$$Q_M = I$$

$$\phi_M = ( |1 - \frac{1}{2}j\omega N_0| )^{-M} = (1 - \frac{1}{2}j\omega N_0)^{-M}$$

$$p_2(q) = (2\pi)^{-1} \int_{-\infty}^{\infty} \phi_M(\omega) \text{EXP}(-j\omega q) d\omega = (2\pi)^{-1} \int_{-\infty}^{\infty} \frac{\text{EXP}(-j\omega q)}{(1 - \frac{1}{2}j\omega N_0)^{-M}} d\omega$$

$$= (2/N_0)^M q^{M-1} \text{EXP}(-2q/N_0) / \Gamma(M) U(q)$$

The probability of false alarm is then:

$$P_{FA} = \int_{\gamma}^{\infty} p_2(q) dq = (2/N_0)^M (1/\Gamma(M)) \int_{\gamma}^{\infty} q^{M-1} \text{EXP}(-2q/N_0) dq$$

$$= \text{EXP}(-2\gamma/N_0) \sum_{m=0}^{M-1} (m!)^{-1} (2\gamma/N_0)^m \quad \gamma > 0$$

where  $\Gamma(M)$  is the Gamma Function, i.e.  $\Gamma(M) = (M-1)!$

### APPENDIX A.3 Distribution of Monopulse Statistics.

The sum and difference channels,  $\Sigma$  and  $\Delta$  are correlated complex gaussian random processes. The joint probability density function of simultaneous samples from the two processes is given by:

$$p(\Sigma, \Delta) = (2\pi)^{-2} |\Lambda|^{-1} \exp(-\frac{1}{2} (\Sigma^* \Delta^*) \Lambda^{-1} \begin{pmatrix} \Sigma \\ \Delta \end{pmatrix})$$

$$= \frac{1}{2} \begin{pmatrix} \mu_1 & \rho \\ \rho & \mu_2 \end{pmatrix} \quad \text{as defined in Section 3.2.1}$$

$$\Lambda^{-1} = (2|\Lambda|)^{-1} \begin{pmatrix} \mu_1 & -\rho \\ -\rho & \mu_2 \end{pmatrix} = \begin{pmatrix} \beta_{11} & \beta_{12} \\ \beta_{21} & \beta_{22} \end{pmatrix}$$

$$p(\Sigma, \Delta) = (2\pi)^{-2} |\Lambda|^{-1} \exp(-\frac{1}{2} (|\Sigma|^2 \beta_{11} + |\Delta|^2 \beta_{22} + 2\beta_{12} \text{Re}(\Sigma \Delta^*)))$$

A change of variables can now be done. Let:

$$\begin{aligned} v_1 &= |\Sigma| \\ v_2 &= |\Delta| \\ \phi_1 &= \arg \Sigma \\ \phi_2 &= \arg \Delta \end{aligned}$$

The Jacobian of this transformation is  $J = -(v_1 v_2)^{-1}$

$$p(v_1, v_2, \phi_1, \phi_2) = (2\pi)^{-2} |\Lambda|^{-1} v_1 v_2 \exp(-\frac{1}{2} (\beta_{11} v_1^2 + \beta_{22} v_2^2 + 2\beta_{12} v_1 v_2 \cos(\phi_1 - \phi_2)))$$

Note that this function depends only on  $\phi_1 - \phi_2$  and not on the values of the angles themselves. Defining  $\psi = \phi_1 - \phi_2$  and integrating out one variable yields:

$$p(v_1, v_2, \psi) = (2\pi)^{-1} |\Lambda|^{-1} v_1 v_2 \exp(-\frac{1}{2}(\beta_{11} v_1^2 + \beta_{22} v_2^2 + 2\beta_{12} v_1 v_2 \cos \psi))$$

From this density function, the density of the monopulse channel statistics can be derived. Defining X and Y as the real and imaginary parts respectively of the monopulse channel then:

$$X = \operatorname{Re} \left[ \frac{\sum \Delta^*}{\sum \Sigma^*} \right] = (v_2/v_1) \cos \psi \quad Y = \operatorname{Im} \left[ \frac{\sum \Delta^*}{\sum \Sigma^*} \right] = (v_2/v_1) \sin \psi$$

$$v_2^2 = (X^2 + Y^2) v_1^2$$

$$v_2 \cos \psi = v_1 X$$

The change of variables from  $(v_1, v_2, \psi)$  to  $(X, Y, v_1)$  has Jacobian,  $J = (v_2/v_1^2)$ .

$$p(X, Y, v_1) = (2\pi |\Lambda|)^{-1} v_1^3 \exp(-\frac{1}{2} v_1^2 (\beta_{11} + \beta_{22} (X^2 + Y^2) + 2\beta_{12} X))$$

$$\begin{aligned} p(X, Y) &= p(X, Y, v_1) dv_1 = \pi^{-1} (\beta_{11} + \beta_{22} (X^2 + Y^2) + 2\beta_{12} X)^{-2} \\ &= \frac{\mu_x \mu_y - \rho^2}{(\mu_x + \mu_y (X^2 + Y^2) - 2\rho X)^2} \end{aligned}$$

$$\text{With } m = \rho/\mu_x \quad w^2 = \mu_y/\mu_x - (\rho/\mu_x)^2$$

$$p(X, Y) = \frac{w^2}{\pi (w^2 + m^2 + X^2 + Y^2 - 2mX)^2} = \frac{w^2}{\pi ((X-m)^2 + Y^2 + w^2)^2}$$

Defining  $U = X - m$ :

$$p(U, Y) = \frac{W^2}{\pi (U^2 + Y^2 + W^2)^2}$$

$$p(U) = \int_{-\infty}^{\infty} p(U, Y) dY = \frac{W^2}{2(U^2 + W^2)^{1.5}}$$

$$p(Y) = \int_{-\infty}^{\infty} p(U, Y) dU = \frac{W^2}{2(Y^2 + W^2)^{1.5}}$$

$$E[U] = \int_{-\infty}^{\infty} U p(U) dU = \frac{1}{2} \int_{-\infty}^{\infty} \frac{W^2 U}{(U^2 + W^2)^{1.5}} dU = 0$$

$$E[Y] = \int_{-\infty}^{\infty} Y p(Y) dY = \frac{1}{2} \int_{-\infty}^{\infty} \frac{W^2 Y}{(Y^2 + W^2)^{1.5}} dY = 0$$

$$p(U|Y) = p(U, Y)/p(Y) = \frac{2(W^2 + Y^2)^{1.5}}{\pi (W^2 + Y^2 + U^2)^2}$$

$$E[U|Y] = \int_{-\infty}^{\infty} U p(U|Y) dU = 0$$

$$E[U^2|Y] = \int_{-\infty}^{\infty} U^2 p(U|Y) dU = (2/\pi)(W^2 + Y^2)^{1.5} \int_{-\infty}^{\infty} \frac{U^2}{(W^2 + Y^2 + U^2)^2} dU$$

$$= W^2 + Y^2$$

$$\sigma_{U|Y}^2 = E[U^2|Y] - E^2[U|Y] = W^2 + Y^2$$

Data will be thresholded on Y, discarding all data when  $|Y| \geq Y_T$ . The variance of the monopulse estimates for the data retained is:



$$\begin{aligned}
\sigma_{U|Y \geq Y_T}^2 &= \frac{\int_{-Y_T}^{Y_T} \sigma_{U|Y}^2 p(Y) dY}{\int_{-Y_T}^{Y_T} p(Y) dY} = \frac{\int_0^{Y_T} (w^2 + Y^2)^{-1/2} dY}{\int_0^{Y_T} (w^2 + Y^2)^{-1.5} dY} \\
&= w^2 (1 + (w/Y_T)^2) \ln((Y_T/w) + \sqrt{1 + (Y_T/w)^2})
\end{aligned}$$

#### APPENDIX A.4 High SNR Approximation to $w^2$ .

From Section 3.2.1 the width parameter  $w^2$  is:

$$w^2 = \mu_v / \mu_z - (\rho / \mu_z)^2$$

For a target with RCS centroid on the boresite  $\rho = 0$ :

$$w^2 = \mu_v / \mu_z = \frac{\int \theta^2 S(\theta) d\theta + N_o / 2b^2}{\int S(\theta) d\theta + N_o / 2a^2}$$

With high SNR, i.e.,  $\int S(\theta) d\theta \gg N_o / 2a^2$

$$w^2 = \frac{\int \theta^2 S(\theta) d\theta}{\int S(\theta) d\theta} + \frac{N_o}{2b^2 \int S(\theta) d\theta}$$

Recognizing that the first term is the noise free width parameter,  $w_o^2$ , and the second term is related to the sum channel SNR:

$$\text{SNR} = \frac{2a^2 \int S(\theta) d\theta}{N_o}$$

Then it is possible to approximate  $w^2$  as:

$$w^2 = w_o^2 + (a^2/b^2) \text{SNR}^{-1}$$

Assume a quadratic beam shape,  $f_{\pm}(\phi) = 1 - 1.17(\phi - \phi_{BW}/2)^2 / \phi_{BW}^2$ , where  $\phi_{BW}$  is the 3-db beamwidth and the beams cross at the 3-db points.

$$a = f_{\pm}(0) = 0.707$$

$$b = |f'_{\pm}(0)| = 1.17/\phi_{BW}$$

$$w^2 = w_o^2 + 0.365 \phi_{BW}^2 \text{SNR}^{-1}$$

# APPENDIX A.5 Maximum Likelihood Estimation of Monopulse Angle for Rayleigh Scatterer.

The sum and difference channels,  $\Sigma$  and  $\Delta$ , are correlated gaussian random variables with density as given in Appendix A.3 when the target is a Rayleigh scatterer. Assume that M pulses have been transmitted and the data consists of M samples of each channel,  $\Sigma_k, \Delta_k, k=1,2,\dots,M$ . Each data sample is complex and it is assumed that there is no pulse-to-pulse correlation. The joint probability density function of receiving all the data is:

$$p(\Sigma_k, \Delta_k; k=1,2,\dots,M) = (2\pi)^{-2M} |\Lambda|^{-M} \exp\left(-\frac{1}{2} \sum_{k=1}^M (\Sigma_k^* \Delta_k^*) \Lambda^{-1} \begin{pmatrix} \Sigma_k \\ \Delta_k \end{pmatrix}\right)$$

$$\Lambda = \frac{1}{2} \begin{pmatrix} \mu_\Sigma & \rho \\ \rho & \mu_\Delta \end{pmatrix}$$

When there is no noise, the matrix  $\Lambda$  can be written:

$$\Lambda = \frac{1}{2} \begin{pmatrix} 1 & m \\ m & W^2 + m^2 \end{pmatrix}$$

where m and W are as defined in Section 3.2.1 and  $\mu_0 = \mu_\Sigma$  where:  $N_0 = 0$ , i.e.  $\mu_0 = \int S(\theta) d\theta$ . The maximum likelihood estimate of m is the value which maximizes the probability density function. That is one must find the value of m which satisfies the following expression:

$$\frac{\partial}{\partial m} \left\{ \sum_{k=1}^M (\Sigma_k^* \Delta_k^*) \begin{pmatrix} m^2 + W^2 & -m \\ -m & 1 \end{pmatrix} \begin{pmatrix} \Sigma_k \\ \Delta_k \end{pmatrix} \right\}_{m=\hat{m}} = 0$$

$$\sum_{k=1}^M \left( \sum_k^* \Delta_k^* \right) \begin{pmatrix} 2m & -1 \\ -m & 0 \end{pmatrix} \begin{pmatrix} \sum_k \\ \Delta_k \end{pmatrix} \bigg|_{m=\hat{m}} = 0$$

$$2\hat{m} \sum_{k=1}^M |\Sigma_k|^2 = \sum_{k=1}^M \left( \sum_k \Delta_k^* + \sum_k^* \Delta_k \right)$$

$$\begin{aligned} \hat{m} &= \frac{\sum_{k=1}^M \operatorname{Re}(\sum_k \Delta_k^*)}{\sum_{k=1}^M |\Sigma_k|^2} \\ \hat{m} &= \frac{\sum_{k=1}^M |\Sigma_k|^2 \frac{\operatorname{Re}(\sum_k \Delta_k^*)}{|\Sigma_k|^2}}{\sum_{k=1}^M |\Sigma_k|^2} \\ &= \sum_{k=1}^M w_k \frac{\operatorname{Re}(\sum_k \Delta_k^*)}{|\Sigma_k|^2} \end{aligned}$$

$$\text{where } w_k = \frac{|\Sigma_k|^2}{\sum_{k=1}^M |\Sigma_k|^2}$$

It is easy to see that if the k-th monopulse channel angle estimate is called  $x_k$ :

$$x_k = \frac{\operatorname{Re}(\sum_k \Delta_k^*)}{|\Sigma_k|^2}$$

$$\hat{m} = \frac{\sum_{k=1}^M |\Sigma_k|^2 x_k}{\sum_{k=1}^M |\Sigma_k|^2}$$

i.e. the best estimate of the angle given many independent monopulse angle estimates is the RCS weighted sum of the single pulse angle estimates. This also demonstrates that for a single pulse of data, the conventional monopulse angle estimate is optimum under the assumptions made.

The next step is to find the mean and variance of  $\hat{m}$ :

$$\hat{m} = \frac{\sum_{k=1}^M \operatorname{Re}(\sum_k \Delta_k^*)}{\sum_{k=1}^M |\Sigma_k|^2}$$

Since  $\sum_k, \Delta_k$  are gaussian with covariance matrix  $\Lambda$ ,

$$\Lambda = \frac{1}{2} \begin{pmatrix} \mu_o & \mu_o^m \\ \mu_o^m & \mu_o(w^2 + m^2) \end{pmatrix}$$

$$E[\Delta_k | \Sigma_k] = \sum_k \frac{E[\sum_k \Delta_k^*]}{E[|\Sigma_k|^2]} = m \sum_k \quad *$$

$$E[|\Delta_k|^2 | \Sigma_k] = E[|\Delta_k|^2] - \frac{E^2[\sum_k \Delta_k^*]}{E[|\Sigma_k|^2]} + E^2[\Delta_k | \Sigma_k] \quad *$$

$$= \mu_o(w^2 + m^2) - \mu_o^m^2 + m^2 |\Sigma_k|^2$$

\* These equations are well known and derived from the orthogonality prin.

$$= \mu_o w^2 + m^2 |\Sigma_k|^2$$

$$\sigma_{\Delta_k|\Sigma_k}^2 = E[|\Delta_k|^2|\Sigma_k] - E^2[\Delta_k|\Sigma_k] = \mu_o w^2$$

$$E[\hat{m}|\Sigma_k; k=1,2,\dots,M] = \frac{\sum_{k=1}^M \operatorname{Re}(\Sigma_k E[\Delta_k^*|\Sigma_k])}{\sum_{k=1}^M |\Sigma_k|^2} = m$$

$$\sigma_{\hat{m}|\Sigma_k}^2 = E[(m - \hat{m})^2|\Sigma_k; k=1,2,\dots,M]$$

$$= E\left\{ \frac{\sum_k (\Sigma_k (\Delta_k^* - m) + \Sigma_k^* (\Delta_k - m))^2}{2 \sum_k |\Sigma_k|^2} \middle| \Sigma_k; k=1,2,\dots,M \right\}$$

$$= \frac{(\sum_k |\Sigma_k|^2) \mu_o w^2}{2(\sum_k |\Sigma_k|^2)^2} = \frac{1}{2} \frac{\mu_o w^2}{\sum_k |\Sigma_k|^2}$$

Let  $q = \sum_{k=1}^M |\Sigma_k|^2$ . Note that  $q$  is chi-square order  $2M$ .

$$p(q) = (\mu_o^M (M-1)!)^{-1} q^{M-1} \exp(-q/\mu_o) \quad q > 0$$

$$\sigma_{\hat{m}}^2 = \frac{1}{2} \int_0^\infty (\mu_o w^2/q) p(q) dq = w^2/(2(M-1)!) \int_0^\infty (q/\mu_o)^{M-2} \exp(-q/\mu_o) \frac{dq}{\mu_o}$$

$$= w^2/(2(M-1))$$

